

ALPS: The Arbitrary Linear Plasma Solver

D. Verscharen^{1,2†}, K. G. Klein^{3,4}, B. D. G. Chandran^{2,5},
M. L. Stevens⁶, C. S. Salem⁷, and S. D. Bale^{7,8}

¹Mullard Space Science Laboratory, University College London, Dorking RH5 6NT, UK

¹Space Science Center, University of New Hampshire, Durham, NH 03824, USA

³Department of Climate and Space Sciences and Engineering, University of Michigan, Ann Arbor, MI 48109, USA

⁴Lunar and Planetary Laboratory, University of Arizona, Tucson, AZ 85719, USA

⁵Department of Physics, University of New Hampshire, Durham, NH 03824, USA

⁶Harvard Smithsonian Center for Astrophysics, Cambridge, MA 02138, USA

⁷Space Sciences Laboratory, University of California, Berkeley, CA 94720, USA

⁸Department of Physics, University of California, Berkeley, CA 94720, USA

(Received xx; revised xx; accepted xx)

The Arbitrary Linear Plasma Solver (ALPS) is a parallelised numerical code that solves the dispersion relation in a hot (even relativistic) magnetised plasma with an arbitrary number of particle species with arbitrary gyrotropic equilibrium distribution functions for any direction of wave propagation with respect to the background field. ALPS reads the background momentum distributions as tables of values on a $(p_{\perp}, p_{\parallel})$ grid, where p_{\perp} and p_{\parallel} are the momentum coordinates in the directions perpendicular and parallel to the background magnetic field, respectively. We present the mathematical and numerical approach used by ALPS and introduce our algorithms for the handling of poles and the analytic continuation for the Landau contour integral. We then show test calculations of dispersion relations for a selection of stable and unstable configurations in Maxwellian, bi-Maxwellian, κ -distributed, and Jüttner-distributed plasmas. These tests demonstrate that ALPS derives reliable plasma dispersion relations. ALPS will make it possible to determine the properties of waves and instabilities in the non-equilibrium plasmas that are frequently found in space, laboratory experiments, and numerical simulations.

1. Introduction

The vast majority of the visible matter in the universe is in the plasma state. The solar wind is an example of such an astrophysical plasma. Due to its accessibility to spacecraft, it is the perfect environment for making comparisons between theoretical plasma-physics predictions and in-situ observations in the astrophysical context with access to wide scale separations (see, for example, Marsch 2006). Plasma can deviate from thermodynamic equilibrium if the relaxation due to particle collisions occurs on timescales that are larger than the characteristic timescales of the collective plasma behaviour. Such a *collisionless plasma* is characterised by non-Maxwellian features in its velocity distribution functions. In the fast solar wind, this condition is frequently fulfilled, and, consequently, the observed distribution functions often deviate from the entropically favoured Maxwellian shape (Vasyliunas 1968; Gosling *et al.* 1981; Lui & Krimigis 1981; Marsch *et al.* 1982*b,a*; Armstrong *et al.* 1983; Lui & Krimigis 1983; Christon *et al.* 1988; Williams *et al.* 1988). In particular, beams and temperature anisotropies are some of the observed features in

† Email address for correspondence: d.verscharen@ucl.ac.uk

the distributions of ions and electrons in the solar wind (Pilipp *et al.* 1987*a,b*; Hellinger *et al.* 2006; Marsch 2006; Bale *et al.* 2009). If these deviations from equilibrium are suitably extreme, the plasma becomes unstable and generates waves or non-propagating structures that react back upon the plasma to reduce the deviations from equilibrium (Eviatar & Schulz 1970; Schwartz 1980; Gary 1993; Hellinger & Trávníček 2011, 2013).

The behaviour of plasma waves and instabilities is typically studied with the help of numerical codes that solve the hot-plasma dispersion relation. Traditionally, these codes (like WHAMP, PLUME, or NHDS) use a shifted bi-Maxwellian background distribution function as the zeroth-order description for the plasma state (Roennmark 1982; Quataert 1998; Klein *et al.* 2012; Verscharen *et al.* 2013*a*). For nearly collisionless plasmas, however, the bi-Maxwellian distribution function is a mathematical convenience rather than a reliable representation of the true plasma distribution function, and many space-plasma observations show that the bi-Maxwellian representation is not accurate (Hundhausen 1970; Leubner 1978; Marsch *et al.* 1982*b*; Pilipp *et al.* 1987*a*; Marsch & Tu 2001; Štverák *et al.* 2009). Some previous approaches in non-Maxwellian solvers treated certain limits or geometries (Dum *et al.* 1980; Summers & Thorne 1991; Summers *et al.* 1994; Xue *et al.* 1993, 1996; Hellberg *et al.* 2005; Cattae *et al.* 2007; Lazar, M. & Poedts, S. 2009; Mace & Sydora 2010; Lazar *et al.* 2011; Galvañ *et al.* 2012; Xie 2013; Lazar & Poedts 2014; Gaelzer & Ziebell 2016; Gaelzer *et al.* 2016) or faced challenges in the weakly-damped limit (Hellinger & Trávníček 2011).

We present our numerical code ALPS (Arbitrary Linear Plasma Solver), which solves the full hot-plasma dispersion relation in a plasma consisting of an arbitrary number of particle species with arbitrary background distribution functions f_{0j} and with arbitrary directions of wave propagation with respect to the uniform background magnetic field. ALPS is also able to solve the dispersion relation for relativistic plasmas. Matsuda & Smith (1992) developed a code similar to ALPS that calculates the dispersion relation in an arbitrary plasma with relativistic effects. Their code uses a cubic spline fit to both fill data gaps and approximate the analytic continuation, while ALPS uses a novel method called *hybrid analytic continuation*. The spline method forfeits its accuracy for strongly damped solutions since the calculation of the dispersion relation requires the evaluation of the spline at a complex value that is distant from the real grid points by which the spline is supported. Our method does not suffer from this problem. Astfalk & Jenko (2017) also use a cubic-spline interpolation for the analytic continuation and as the basis for the integration in their code LEOPARD. This procedure allows for algebraic simplifications that enhance the speed of the integration significantly. LEOPARD, however, does not capture relativistic effects.

In Section 2, we review the underlying theory of the hot-plasma dispersion relation. Section 3 presents ALPS's numerical approach. In Section 4, we compare ALPS results to known limits of the hot-plasma dispersion relation such as Maxwellian, bi-Maxwellian, κ -distributed, and relativistic pair plasmas. In Section 5, we discuss our results and the applicability of ALPS to measured plasma distributions. The Appendix describes how ALPS solutions depend on the resolution of the background distributions, discusses of the Levenberg-Marquardt-fit routine used in our hybrid-analytic-continuation method, and describes our strategy for numerically refining coarse-grained distribution functions obtained from spacecraft measurements.

2. The Linear Dispersion Relation of a Hot Plasma

In this section, we discuss the mathematical basis for the calculation of the hot-plasma dispersion relation following the presentation and notation of Stix (1992). The

determination of the kinetic wave dispersion relation in a hot plasma is based on the linearised set of Maxwell's equations and the linearised Vlasov equation (Stix 1992; Gary 1993). A wave or instability is then associated with a first-order perturbation δf_j in the distribution function of species j about a prescribed time-averaged background distribution function f_{0j} ,

$$f_j(\mathbf{x}, \mathbf{p}, t) = f_{0j}(\mathbf{p}) + \delta f_j(\mathbf{x}, \mathbf{p}, t), \quad (2.1)$$

where \mathbf{x} is the spatial coordinate and \mathbf{p} is the momentum coordinate. As with the distribution function f_j in Equation (2.1), we take the magnetic field \mathbf{B} to be the sum of a uniform background magnetic field \mathbf{B}_0 and a fluctuating magnetic field $\delta\mathbf{B}$. We assume that $\mathbf{E} = \delta\mathbf{E}$; i.e., the average electric field is zero. Linear theory expresses δf_j as a function of f_{0j} and the electromagnetic field components.

The distribution function f_j in a collisionless plasma evolves according to the Vlasov equation,

$$\frac{\partial f_j}{\partial t} + \mathbf{v} \cdot \frac{\partial f_j}{\partial \mathbf{r}} + q_j \left(\mathbf{E} + \frac{\mathbf{v}}{c} \times \mathbf{B} \right) \cdot \frac{\partial f_j}{\partial \mathbf{p}} = 0, \quad (2.2)$$

where q_j is the charge of a particle of species j , c is the speed of light, and \mathbf{v} is the velocity coordinate. We assume that all fluctuating quantities behave like plane waves; i.e., $\propto \exp(i\mathbf{k} \cdot \mathbf{x} - i\omega t)$, where \mathbf{k} is the wave vector and ω is the (complex) frequency. Linearising Equation (2.2), using Faraday's law, and applying the method of characteristics, we obtain

$$\delta f_j = -q_j e^{i\mathbf{k} \cdot \mathbf{r} - i\omega t} \int_0^\infty d\tau e^{i\alpha} \left\{ E_x U \cos(\phi + \Omega_j \tau) + E_y U \sin(\phi + \Omega_j \tau) + E_z \left[\frac{\partial f_{0j}}{\partial p_{\parallel}} - V \cos(\phi - \vartheta + \Omega_j \tau) \right] \right\}, \quad (2.3)$$

where $\mathbf{E} = (E_x, E_y, E_z)$ is the electric field, ϕ is the azimuthal angle of the momentum vector \mathbf{p} , ϑ is the azimuthal angle of the wavevector \mathbf{k} , and the index \perp (\parallel) refers to the direction perpendicular (parallel) with respect to the background magnetic field \mathbf{B}_0 ,

$$\Omega_j \equiv \frac{q_j B_0}{m_j c \sqrt{1 + (p_{\perp}^2 + p_{\parallel}^2) / m_j^2 c^2}} \quad (2.4)$$

is the relativistic gyrofrequency, m_j is the rest mass of a particle of species j ,

$$\alpha \equiv -\frac{k_{\perp} v_{\perp}}{\Omega_j} [\sin(\phi - \vartheta + \Omega_j \tau) - \sin(\phi - \vartheta)] + (\omega - k_{\parallel} v_{\parallel}) \tau, \quad (2.5)$$

$$U \equiv \frac{\partial f_{0j}}{\partial p_{\perp}} + \frac{k_{\parallel}}{\omega} \left(v_{\perp} \frac{\partial f_{0j}}{\partial p_{\parallel}} - v_{\parallel} \frac{\partial f_{0j}}{\partial p_{\perp}} \right), \quad (2.6)$$

and

$$V \equiv \frac{k_{\perp}}{\omega} \left(v_{\perp} \frac{\partial f_{0j}}{\partial p_{\parallel}} - v_{\parallel} \frac{\partial f_{0j}}{\partial p_{\perp}} \right). \quad (2.7)$$

The first velocity moments of the distribution functions of all species define the current density \mathbf{j} through

$$\mathbf{j} = \sum_j q_j \int d^3 \mathbf{p} \mathbf{v} \delta f_j = -\frac{i\omega}{4\pi} \sum_j \chi_j \cdot \mathbf{E}, \quad (2.8)$$

where χ_j is the contribution of species j to the plasma susceptibility. Without loss of generality, we choose a cylindrical coordinate system in which $k_y = \vartheta = 0$ and apply a set of Bessel-function identities in order to facilitate the integration over ϕ and τ in Equation (2.3). This allows us to rewrite the plasma susceptibilities as (provided that $\text{Im}(\omega) > 0$)

$$\chi_j = \frac{\omega_{pj}^2}{\omega\Omega_{0j}} \int_0^\infty 2\pi p_\perp dp_\perp \int_{-\infty}^{+\infty} dp_\parallel \left[\hat{\mathbf{e}}_\parallel \hat{\mathbf{e}}_\parallel \frac{\Omega_j}{\omega} \left(\frac{1}{p_\parallel} \frac{\partial f_{0j}}{\partial p_\parallel} - \frac{1}{p_\perp} \frac{\partial f_{0j}}{\partial p_\perp} \right) p_\parallel^2 + \sum_{n=-\infty}^{+\infty} \frac{\Omega_j p_\perp U}{\omega - k_\parallel v_\parallel - n\Omega_j} \mathbf{T}_n \right], \quad (2.9)$$

where $\omega_{pj} \equiv \sqrt{4\pi n_j q_j^2/m_j}$ is the plasma frequency of species j , $\Omega_{0j} \equiv q_j B_0/m_j c$ is the non-relativistic gyrofrequency, n_j is the density of species j , and the tensor \mathbf{T}_n is defined as

$$\mathbf{T}_n \equiv \begin{pmatrix} \frac{n^2 J_n^2}{z^2} & \frac{inJ_n J'_n}{z} & \frac{nJ_n^2 p_\parallel}{z p_\perp} \\ -\frac{inJ_n J'_n}{z} & (J'_n)^2 & -\frac{iJ_n J'_n p_\parallel}{p_\perp} \\ \frac{nJ_n^2 p_\parallel}{z p_\perp} & \frac{iJ_n J'_n p_\parallel}{p_\perp} & \frac{J_n^2 p_\parallel^2}{p_\perp^2} \end{pmatrix}, \quad (2.10)$$

where $z \equiv k_\perp v_\perp/\Omega_j$, and $J_n \equiv J_n(z)$ is the n th-order Bessel function. For $\text{Im}(\omega) \leq 0$, the integral over p_\parallel is executed as the Landau integral after analytic continuation (for details, see Chapt. 8 of Stix 1992). Equation (2.9) describes the susceptibility for a general background distribution function f_{0j} in a relativistic plasma. The only assumptions are gyrotropy in f_{0j} and small amplitudes in the fluctuations so that linearisation is applicable, and a uniform, stationary equilibrium. The numerical challenge in the solution of the plasma dispersion relation results from the integrals over p_\perp and p_\parallel in Equation (2.9). We note that, in numerous classical codes for calculation of the linear hot-plasma dispersion relation (Roennmark 1982; Gary 1993; Verscharen *et al.* 2013b; Klein & Howes 2015), these integrals are greatly simplified by assuming that f_{0j} is a (bi)-Maxwellian.

The dielectric tensor $\boldsymbol{\varepsilon}$ of the plasma is related to the plasma susceptibilities from Equation (2.9) through

$$\boldsymbol{\varepsilon} = \mathbf{1} + \sum_j \chi_j. \quad (2.11)$$

Finally, combining Faraday's law and Ampère's law leads to the wave equation,

$$\mathbf{n} \times (\mathbf{n} \times \mathbf{E}) + \boldsymbol{\varepsilon} \cdot \mathbf{E} \equiv \mathcal{D} \cdot \mathbf{E} = 0, \quad (2.12)$$

where $\mathbf{n} \equiv \mathbf{k}c/\omega$ is the index. By setting $\det \mathcal{D} = 0$, we obtain the dispersion relations $\omega = \omega(\mathbf{k})$ for non-trivial solutions to Equation (2.12). We write these solutions in the form $\omega = \omega_r + i\gamma$, where $\omega_r = \text{Re}(\omega)$ and $\gamma = \text{Im}(\omega)$.

3. Numerical Approach

In order to find the solutions to the hot-plasma dispersion relation, ALPS determines the values of ω_r and γ that solve Equation (2.12) for specified background distributions f_{0j} at a given set of values for \mathbf{k} , m_j , q_j , n_j , and v_A/c , where $v_A \equiv B_0/\sqrt{4\pi n_p m_p}$. ALPS uses an efficient iterative Newton-secant algorithm to solve Equation (2.12) based on an initial guess for ω_r and γ (Press *et al.* 1992). The numerically challenging part for this calculation is the evaluation of χ_j in Eqs. (2.9). In the following, we present ALPS's strategy for this evaluation in the non-relativistic case. We discuss the extension to relativistic cases with poles in the integration domain in Section 3.3, which is equivalent to the non-relativistic case with the exception that the coordinate system is transformed from (p_\perp, p_\parallel) to $(\Gamma, \bar{p}_\parallel)$ and that Equation (3.16) below is used instead of Equation (2.9).

We prescribe the shape of f_{0j} in input files for each species (called “ f_0 table”) as an ASCII table that lists p_\perp , p_\parallel , and the associated values of f_{0j} . From this table, we calculate $\partial f_{0j}/\partial p_\perp$ and $\partial f_{0j}/\partial p_\parallel$ on the same grid as the f_0 table using second-order finite differencing. The resolution of the f_0 table is given by n_\perp points in the p_\perp -direction and n_\parallel points in the p_\parallel -direction. The table spans from $p_\perp = 0$ to $p_\perp = P_{\max, \perp j}$ in the perpendicular direction and from $p_\parallel = -P_{\max, \parallel j}$ to $p_\parallel = P_{\max, \parallel j}$ in the parallel direction.

The integration in Equation (2.9) allows us to integrate separately and independently for each n and j . This provides us with a very natural way to parallelise the calculation scheme by assigning the separate integrations to different processors. We use MPI for the parallelisation. The integrating nodes return their contributions to χ_j to the master node, which then sums up the contributions, determines the value of ε , and updates the values of ω_r and γ through a Newton-secant step. The updated values for ω_r and γ are then returned to the integrating nodes, which afterwards evaluate the integration of their updated contribution to χ_j . We evaluate all values of n up to a value of $\pm n_{\max}$, which is determined as the value of n for which the maximum value of $|J_n|$ is smaller than the user-defined parameter J_{\max} . The necessary value of n_{\max} depends on the wavenumber, the direction of propagation of the treated wave, and the thermal speeds of the plasma components. In bi-Maxwellian codes under typical solar-wind conditions, the accuracy of the dispersion relation is better than $\Delta|\omega|/|\omega| \sim 10^{-5}$ for $J_{\max} \sim 10^{-45}$ (which typically corresponds to $n_{\max} \gtrsim 10$ at proton scales).

We use a standard two-dimensional trapezoidal integration scheme to integrate over p_\perp and p_\parallel . However, this scheme breaks down near the poles of the integrand in Equation (2.9) and requires a special treatment of the analytic continuation when $\gamma \leq 0$. In the remainder of this section, we discuss our strategies to resolve these numerical difficulties.

3.1. Integrating Near Poles

A challenge concerning the numerical integration is the treatment of the poles that occur in the term proportional to \mathbf{T}_n in Equation (2.9). The integrals in question are of the form

$$I(p_\perp) = \int_{-\infty}^{+\infty} dp_\parallel \frac{\Omega_j U \mathbf{T}_n}{\omega - k_\parallel v_\parallel - n\Omega_j} \equiv \int_{-\infty}^{+\infty} dp_\parallel G(p_\perp, p_\parallel) \quad (3.1)$$

for $\gamma > 0$. For sufficiently small γ , the denominator in Equation (3.1) can become very small along the real p_\parallel axis so that the grid sampling leads to large numerical errors in the integration. To describe how we evaluate these integrals, we first rewrite the integral

in Equation (3.1) in the more generic form

$$\mathcal{I} = \int_{-\infty}^{+\infty} dx \frac{g(x)}{x - t_r - it_i}, \quad (3.2)$$

where x , t_r , and t_i are real, $g(x)$ is a smooth function, and the integration is performed along the real axis. We choose a symmetric interval $[t_r - \Delta, t_r + \Delta]$ around t_r where $\Delta \ll g(t_r)/g'(t_r)$, and write

$$\mathcal{I} = \int_{t_r - \Delta}^{t_r + \Delta} dx \frac{g(x)}{x - t_r - it_i} + \text{rest}, \quad (3.3)$$

where “rest” refers to the integration outside the interval $[t_r - \Delta, t_r + \Delta]$. We define a function $f(x)$ to be odd with respect to t_r if $f(x) = -f(2t_r - x)$, and even with respect to t_r if $f(x) = f(2t_r - x)$. Following Longman (1958) and Davis & Rabinowitz (1984), we then separate the integrand into its odd and even parts with respect to t_r as

$$\begin{aligned} \mathcal{I} = \frac{1}{2} \int_{t_r - \Delta}^{t_r + \Delta} dx \left[\frac{g(x)}{x - t_r - it_i} - \frac{g(2t_r - x)}{-x + t_r - it_i} \right] \\ + \frac{1}{2} \int_{t_r - \Delta}^{t_r + \Delta} dx \left[\frac{g(x)}{x - t_r - it_i} + \frac{g(2t_r - x)}{-x + t_r - it_i} \right] + \text{rest}. \end{aligned} \quad (3.4)$$

The integrand in the first integral in Equation (3.4) is odd with respect to t_r and thus vanishes after the integration over the symmetric interval around t_r . The second integral, on the other hand, is even with respect to t_r and thus

$$\mathcal{I} = \int_{t_r}^{t_r + \Delta} dx \left[\frac{g(x)}{x - t_r - it_i} - \frac{g(2t_r - x)}{x - t_r + it_i} \right] + \text{rest}. \quad (3.5)$$

We define Δ through a user-defined parameter n_I so that $\Delta \equiv n_I \Delta p_{\parallel}$. We then define $\delta \equiv \Delta/n_P$, where n_P is another user-defined parameter. Except for cases in which $|t_i|$ is extremely small, we apply a trapezoidal integration over n_P steps of width δ to the integral in Equation (3.5). The smoothness of $g(x)$ allows us to expand $g(x)$ around the nearest grid point of the n_I grid points in the interval $[t_r, t_r + \Delta]$ using a Taylor series. By taking Δp_{\parallel} to be sufficiently small, we can retain just the first two terms in the series without losing significant accuracy. Since the integral in Equation (3.5) does not converge numerically if $|t_i|$ is extremely small, we implement the following procedure when $|t_i| \leq t_{\text{lim}}$, where t_{lim} is a user-defined parameter. We first rewrite Equation (3.5) using truncated Taylor expansions of $g(x)$ and $g(2t_r - x)$ around $x = t_r$ as

$$\mathcal{I} = \int_{t_r}^{t_r + \Delta} dx \left[\frac{2it_i g(t_r)}{(x - t_r)^2 + t_i^2} + \frac{2g'(t_r)(x - t_r)^2}{(x - t_r)^2 + t_i^2} \right] + \text{rest}. \quad (3.6)$$

We determine $g(t_r)$ and $g'(t_r)$ through linear interpolation between the neighbouring grid points to t_r . The term proportional to $g'(t_r)$ in Equation (3.6) converges numerically for

any value of t_i . We set the term proportional to $g(t_r)$ equal to its small- t_i limit, namely

$$\int_{t_r}^{t_r+\Delta} dx \frac{2it_i g(t_r)}{(x-t_r)^2 + t_i^2} = i\pi g(t_r) \text{sgn}(t_i). \quad (3.7)$$

We use this method for both the integration of χ_j near poles and the principal-value integration that is necessary if $\gamma = 0$.

3.2. Analytic Continuation

If $\gamma \leq 0$, the integration in Equation (2.9) requires an analytic continuation into the complex plane. If f_{0j} were given as a closed algebraic expression, the analytic continuation would simply entail the evaluation of $f_{0j}(p_\perp, p_\parallel)$ at a complex value for p_\parallel in the non-relativistic case. In our case, however, f_{0j} is only defined on a real grid in p_\perp and p_\parallel , yet the analytic continuation of f_{0j} is still uniquely defined. This leads to the known mathematical problem of *numerical analytic continuation* (Cannon & Miller 1965; Reichel 1986; Fujiwara *et al.* 2007; Fu *et al.* 2012; Zhang Z.-Q. Ma 2013; Kranich 2014). Our solution for this problem is our *hybrid analytic continuation* scheme. We note that this approach is only relevant for damped modes, i.e., $\gamma \leq 0$.

Landau's rule of integration around singularities (Landau 1946; Lifshitz & Pitaevskii 1981) leads to the following three cases with the appropriate residues for the evaluation of $I(p_\perp)$ for general γ :

$$I(p_\perp) = \int_{C_L} dp_\parallel G(p_\perp, p_\parallel) = \begin{cases} \int_{-\infty}^{+\infty} dp_\parallel G(p_\perp, p_\parallel) & \text{if } \gamma > 0, \\ \mathcal{P} \int_{-\infty}^{+\infty} dp_\parallel G(p_\perp, p_\parallel) + i\pi \sum \text{Res}_A(G) & \text{if } \gamma = 0, \\ \int_{-\infty}^{+\infty} dp_\parallel G(p_\perp, p_\parallel) + 2i\pi \sum \text{Res}_A(G) & \text{if } \gamma < 0, \end{cases} \quad (3.8)$$

where C_L is the contour of the Landau integration, which lies below the complex poles in the integrand. The integrations on the right-hand side of Equation (3.8) are performed along the real axis, and \mathcal{P} indicates the principal-value integral. The sum sign indicates the summation over the residues of all poles A of the function G . In a non-relativistic plasma, G has one simple pole, and thus

$$\sum \text{Res}_A(G) = -\frac{m_j}{|k_\parallel|} \Omega_j U \mathbf{T}_n|_{p_\parallel=p_{\text{pole}}}, \quad (3.9)$$

where $p_{\text{pole}} = m_j(\omega - n\Omega_j)/k_\parallel$ is the parallel momentum associated with pole A .

It is a common approach to decompose the background distribution functions in terms of analytical expressions and then to evaluate these at the complex poles. Complete orthogonal basis functions such as Hermite, Legendre, or Chebyshev polynomials are the prime candidates for such a decomposition since they can represent f_{0j} to an arbitrary degree of accuracy (Robinson 1990; Weideman 1995; Xie 2013). These approaches are useful when f_{0j} deviates only slightly from a Maxwellian. They require, however, very high orders of decomposition and are thus slow in the presence of typical structures that we see in the solar wind such as a proton core-beam configuration. Therefore, they are unsuitable for ALPS's purpose, and we pursue a different approach, which we call the *hybrid analytic continuation*. The basic idea behind this approach is to integrate I numerically along the real axis whenever possible and to resort to an algebraic function for the sole purpose of the evaluation of $\text{Res}_A(G)$ when necessary.

For the determination of an appropriate algebraic function, ALPS allows the user to choose an arbitrary combination of fit functions to represent f_{0j} and automatically evaluates the fits before the integration begins. The code evaluates the fits separately at each p_{\perp} , so that no assumption is made as to the structure of f_{0j} in the p_{\perp} -direction. ALPS uses these functions only if a pole is within the integration domain and only if $\gamma \leq 0$. The intrinsic fit functions that the code can combine include a Maxwellian distribution,

$$f_{0j} = \frac{n_j}{\pi^{3/2} m_j^3 w_{\perp j}^2 w_{\parallel j}} \exp \left(-\frac{p_{\perp}^2}{m_j^2 w_{\perp j}^2} - \frac{(p_{\parallel} - m_j U_j)^2}{m_j^2 w_{\parallel j}^2} \right), \quad (3.10)$$

where $w_{\perp j} \equiv \sqrt{2k_B T_{\perp j}/m_j}$ ($w_{\parallel j} \equiv \sqrt{2k_B T_{\parallel j}/m_j}$) is the thermal speed of species j in the direction perpendicular (parallel) with respect to \mathbf{B}_0 , $T_{\perp j}$ ($T_{\parallel j}$) is the temperature of species j perpendicular (parallel) to \mathbf{B}_0 , k_B is the Boltzmann constant, and U_j is the \mathbf{B}_0 -parallel drift speed of species j ; a κ -distribution (Summers *et al.* 1994; Astfalk *et al.* 2015),

$$f_{0j} = \frac{n_j}{m_j^3 w_{\perp j}^2 w_{\parallel j}} \left[\frac{2}{\pi(2\kappa - 3)} \right]^{3/2} \frac{\tilde{\Gamma}(\kappa + 1)}{\tilde{\Gamma}(\kappa - 1/2)} \times \left\{ 1 + \frac{2}{2\kappa - 3} \left[\frac{p_{\perp}^2}{m_j^2 w_{\perp j}^2} + \frac{(p_{\parallel} - m_j U_j)^2}{m_j^2 w_{\parallel j}^2} \right] \right\}^{-(\kappa+1)}; \quad (3.11)$$

and a Jüttner distribution (Jüttner 1911; Chacón-Acosta *et al.* 2010),

$$f_{0j} = \frac{n_j}{2\pi m_j^3 c w_j^2 K_2(w_j^2/2c^2)} \exp \left(-2 \frac{c^2}{w_j^2} \sqrt{1 + \frac{|\mathbf{p}|^2}{m_j^2 c^2}} \right); \quad (3.12)$$

where κ is the κ -index, $\tilde{\Gamma}$ is the gamma function, and K_2 is the modified Bessel function of the second kind. The Jüttner distribution is the thermodynamic-equilibrium distribution if $k_B T_j \gtrsim m_j c^2$. The exponential in Equation (3.12) reduces to the Maxwellian $\exp(-v^2/w_j^2)$ with a different \mathbf{p} -independent normalisation factor for $p^2/m_j^2 c^2 \ll 1$. We use an automated Levenberg–Marquardt-fit algorithm (Levenberg 1944; Marquardt 1963) and describe the details of the fit routine in Appendix B.

3.3. The Poles in a Relativistic Plasma

The analytic continuation and pole handling in the relativistic case entail a further complication due to the non-trivial \mathbf{p} -dependence of the resonant denominator in Equation (2.9) (Buti 1962; Lerche 1968). We define a plasma to be relativistic when there is a significant number of particles at relativistic velocities. This can be the case in plasmas with relativistic temperatures ($k_B T_j \gtrsim m_j c^2$) or in plasmas with relativistic beams ($P_j \gtrsim m_j c$, where P_j is the drift momentum). Using the relativistic expression for Ω_j in Equation (2.4) shows that we can write for the pole of the function under the integral sign in Equation (3.1)

$$\frac{1}{\omega - k_{\parallel} v_{\parallel} - n \Omega_j} = -\frac{1}{k_{\parallel}} \frac{\Gamma m_j}{\left(p_{\parallel} - \frac{\omega}{k_{\parallel}} \Gamma m_j + n \frac{\Omega_{0j}}{k_{\parallel}} m_j \right)}, \quad (3.13)$$

where

$$\Gamma \equiv \sqrt{1 + \frac{p_{\perp}^2 + p_{\parallel}^2}{m_j^2 c^2}} \quad (3.14)$$

is the Lorentz factor. We define the dimensionless parallel momentum $\bar{p}_{\parallel} \equiv p_{\parallel}/m_j c$. The dimensionless parallel momentum associated with the relativistic pole is given by

$$\bar{p}_{\text{pole}} = \Gamma \frac{\omega}{k_{\parallel} c} - \frac{n\Omega_{0j}}{k_{\parallel} c}. \quad (3.15)$$

We apply the technique proposed by Lerche (1967) to transform Equation (2.9) from the $(p_{\perp}, p_{\parallel})$ coordinate system to the $(\Gamma, \bar{p}_{\parallel})$ coordinate system (see also Swanson 2002; Lazar & Schlickeiser 2006; López *et al.* 2014, 2016). This transformation yields

$$\begin{aligned} \chi_j = 2\pi m_j^3 c^3 \frac{\omega_{pj}^2}{\omega \Omega_{0j}} \int_1^{\infty} d\Gamma \int_{-\sqrt{\Gamma^2-1}}^{+\sqrt{\Gamma^2-1}} d\bar{p}_{\parallel} \left[\hat{e}_{\parallel} \hat{e}_{\parallel} \frac{\Omega_{0j}}{\omega} \bar{p}_{\parallel} \frac{\partial f_{0j}}{\partial \bar{p}_{\parallel}} \right. \\ \left. - \sum_{n=-\infty}^{+\infty} \frac{\Omega_{0j}}{k_{\parallel} c} \left(\frac{\partial f_{0j}}{\partial \Gamma} + \frac{k_{\parallel} c}{\omega} \frac{\partial f_{0j}}{\partial \bar{p}_{\parallel}} \right) \frac{1}{\bar{p}_{\parallel} - \Gamma \frac{\omega}{k_{\parallel} c} + \frac{n\Omega_{0j}}{k_{\parallel} c}} \bar{\mathbf{T}}_n \right], \quad (3.16) \end{aligned}$$

where

$$\bar{\mathbf{T}}_n \equiv \begin{pmatrix} \frac{n^2 J_n^2}{\bar{z}^2} & \frac{inJ_n J'_n}{\bar{z}} \bar{p}_{\perp} & \frac{nJ_n^2 \bar{p}_{\parallel}}{\bar{z}} \\ -\frac{inJ_n J'_n}{\bar{z}} \bar{p}_{\perp} & (J'_n)^2 \bar{p}_{\perp}^2 & -iJ_n J'_n \bar{p}_{\parallel} \bar{p}_{\perp} \\ \frac{nJ_n^2 \bar{p}_{\parallel}}{\bar{z}} & iJ_n J'_n \bar{p}_{\parallel} \bar{p}_{\perp} & J_n^2 \bar{p}_{\parallel}^2 \end{pmatrix}, \quad (3.17)$$

$\bar{p}_{\perp} \equiv \sqrt{\Gamma^2 - 1 - \bar{p}_{\parallel}^2}$, $\bar{z} \equiv k_{\perp} c / \Omega_{0j}$, and the Bessel functions are evaluated as $J_n \equiv J_n(\bar{z} \bar{p}_{\perp})$. Whenever ALPS performs a relativistic calculation and

$$-P_{\text{max},\parallel j} \leq \text{Re}(p_{\text{pole}}) \leq +P_{\text{max},\parallel j}, \quad (3.18)$$

the code automatically transforms from $(p_{\perp}, p_{\parallel})$ to $(\Gamma, \bar{p}_{\parallel})$ coordinates and applies the polyharmonic spline algorithm described in Appendix C to create an equally spaced and homogeneous grid in $(\Gamma, \bar{p}_{\parallel})$ coordinates. In this coordinate system, we perform the integration near poles and the analytic continuation in the same way as described in Sects. 3.1 and 3.2, but using the relativistic parallel momentum associated with the pole from Equation (3.15). For reasons of numerical performance, we use the integration based on Equation (3.16) only if there is a pole within the integration domain. Otherwise, we employ the faster integration method based on Equation (2.9) even in the relativistic case.

4. Test Cases and Results

In this section, we compare ALPS with known reference cases based on either our own or previously published results.

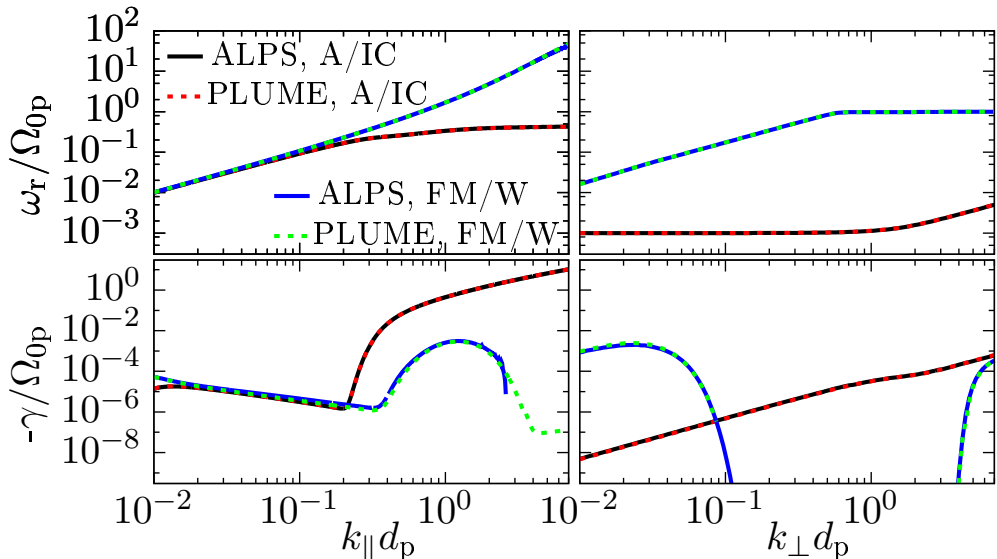


FIGURE 1. Dispersion relations for the A/IC wave and the FM/W wave in a Maxwellian plasma in quasi-parallel (left) and quasi-perpendicular (right) propagation. For the calculations shown on the left, we keep $k_{\perp}d_p = 10^{-3}$ constant and scan through k_{\parallel} . For the calculations shown on the right, we keep $k_{\parallel}d_p = 10^{-3}$ constant and scan through k_{\perp} . The A/IC mode in quasi-perpendicular propagation corresponds to the kinetic Alfvén wave (KAW) at $k_{\perp}d_p \gtrsim 1/\sqrt{\beta_{\parallel p}}$. We compare ALPS with the standard Maxwellian solutions from PLUME for an electron-proton plasma with the same plasma parameters. Both numerical models agree well in both the real part ω_r of the frequency and its imaginary part γ .

4.1. Maxwellian Distributions

There are numerous codes for the hot-plasma dispersion relation in a plasma with Maxwellian or bi-Maxwellian background distributions. We use our code PLUME (Klein & Howes 2015) for an electron-proton plasma and calculate the dispersion relations of Alfvén/ion-cyclotron (A/IC) and fast-magnetosonic/whistler (FM/W) waves. We then set up Maxwellian f_{0j} tables with the same parameters as those used with PLUME and calculate the dispersion relations based on these f_{0j} tables with ALPS. We compare the PLUME and ALPS results for quasi-parallel and quasi-perpendicular propagation in Figure 1. The panels show both the real part of the frequency ω_r and its imaginary part γ as functions of the parallel and perpendicular wavenumbers, respectively. We use $\beta_{\perp j} = \beta_{\parallel j} = 1$ for both protons and electrons, and $v_A/c = 10^{-4}$, where $\beta_{\perp j} \equiv w_{\perp j}^2/v_A^2$ and $\beta_{\parallel j} \equiv w_{\parallel j}^2/v_A^2$. We normalise all frequencies in units of the proton cyclotron frequency Ω_{0p} and all length scales in units of the proton skin depth $d_p \equiv v_A/\Omega_{0p}$. The momentum-space resolution for the ALPS calculation in the quasi-parallel limit is $n_{\perp} = 320$, $n_{\parallel} = 640$, $P_{\max, \parallel p} = 8m_p v_A$, and $P_{\max, \parallel e} = 0.19m_p v_A$. In the quasi-perpendicular limit, we use $n_{\perp} = 240$, $n_{\parallel} = 480$, $P_{\max, \parallel p} = 6m_p v_A$, and $P_{\max, \parallel e} = 0.14m_p v_A$. In both cases, we set $P_{\max, \perp j} = P_{\max, \perp j}$, $J_{\max} = 10^{-45}$, $n_I = 5$, $n_p = 100$, and $T_{\text{lim}} = 0.01$. We study the accuracy of the results depending on the resolution in Appendix A.1. Figure 1 shows that ALPS reproduces these Maxwellian examples very well. We note that these plasma parameters represent typical solar-wind conditions at 1 au.

In order to illustrate another representation of the plasma dispersion relation, we show a comparison of *dispersion maps* from PLUME and ALPS in Figure 2. Dispersion maps are diagrams of isocontours of constant $\lg|\det \mathcal{D}|$, where \mathcal{D} is the tensor from

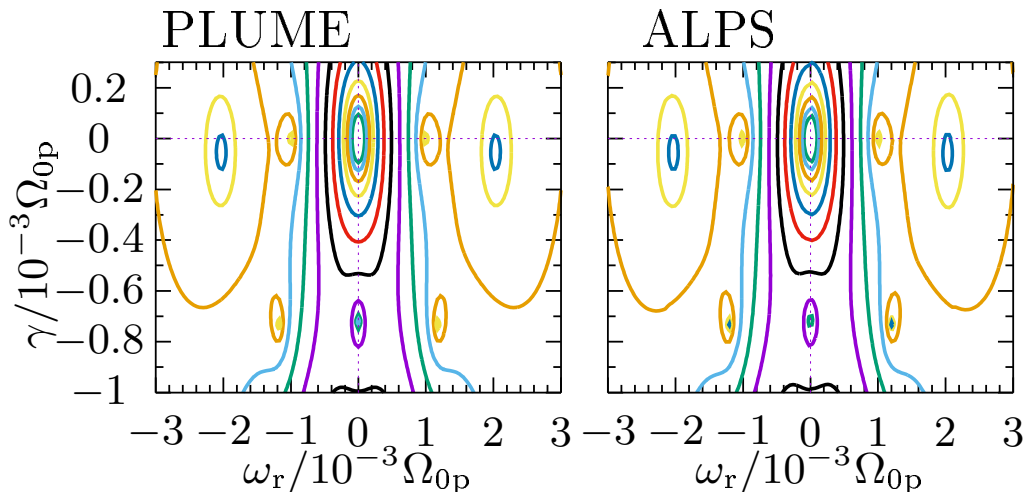


FIGURE 2. Comparison of dispersion maps from PLUME (left) and ALPS (right) for $k_{\perp}d_p = k_{\parallel}d_p = 10^{-3}$. The lines show isocontours of constant $\lg|\det \mathcal{D}|$. Minima in these maps correspond to solutions to the hot-plasma dispersion relation.

Equation (2.12), in the ω_r - γ plane. They are a useful tool to find the initial guesses for ω_r and γ for the Newton-secant root-finding search. Although the calculation of a dispersion map still requires the calculation of all χ_j , it does not entail the application of the Newton-secant root-finding algorithm. Solutions to the hot-plasma dispersion relation appear as minima in these diagrams. We use a Maxwellian plasma model with $\beta_{\perp j} = \beta_{\parallel j} = 1$ for both protons and electrons, $k_{\perp}d_p = k_{\parallel}d_p = 10^{-3}$, and $v_A/c = 10^{-4}$. For the ALPS calculation, we use $n_{\perp} = 240$, $n_{\parallel} = 480$, $P_{\max,\parallel p} = P_{\max,\perp p} = 6m_p v_A$, $P_{\max,\parallel e} = P_{\max,\perp e} = 0.14m_p v_A$, $J_{\max} = 10^{-45}$, $n_I = 5$, $n_p = 100$, and $T_{\text{lim}} = 0.01$. Both the ALPS and the PLUME calculations reveal seven solutions to the dispersion relation. We note that the point $\omega_r = \gamma = 0$ is a maximum and does not represent a solution to the dispersion relation. The solutions at $\omega_r = \pm 10^{-3}\Omega_{0p}$ and $\gamma = -2.3 \times 10^{-10}\Omega_{0p}$ are the forward and backward propagating A/IC waves. The solutions at $\omega_r = \pm 2 \times 10^{-3}\Omega_{0p}$ and $\gamma = -5.4 \times 10^{-5}\Omega_{0p}$ are the forward and backward propagating FM/W waves. The solutions at $\omega_r = \pm 1.2 \times 10^{-3}\Omega_{0p}$ and $\gamma = -7.3 \times 10^{-4}\Omega_{0p}$ are the forward and backward propagating slow waves (ion-acoustic waves). Lastly, the solution at $\omega_r = 0$ and $\gamma = -7.2 \times 10^{-4}\Omega_{0p}$ is the non-propagating slow mode, which is sometimes denoted ‘entropy mode’, (Verscharen *et al.* 2016, 2017). The comparison of both panels in Figure 2 shows that ALPS reproduces these seven plasma modes under typical solar-wind conditions in the Maxwellian limit.

4.2. Anisotropic Bi-Maxwellian Distributions

PLUME, like most other standard hot-plasma dispersion-relation solvers, also allows us to use anisotropic bi-Maxwellian representations for the background distribution functions. Such a configuration can lead to instability if the temperature anisotropy exceeds the threshold for an anisotropy-driven plasma instability. As an example for a propagating instability, we calculate the dispersion relation for the parallel A/IC instability (Harris 1961; Davidson & Ogden 1975; Yoon *et al.* 2010), and as an example for a non-propagating instability, we calculate the dispersion relation for the mirror-mode instability (Rudakov & Sagdeev 1961; Tajiri 1967; Southwood & Kivelson 1993). The thresholds for both of these instabilities fulfil $T_{\perp p} > T_{\parallel p}$. For this demonstration, we

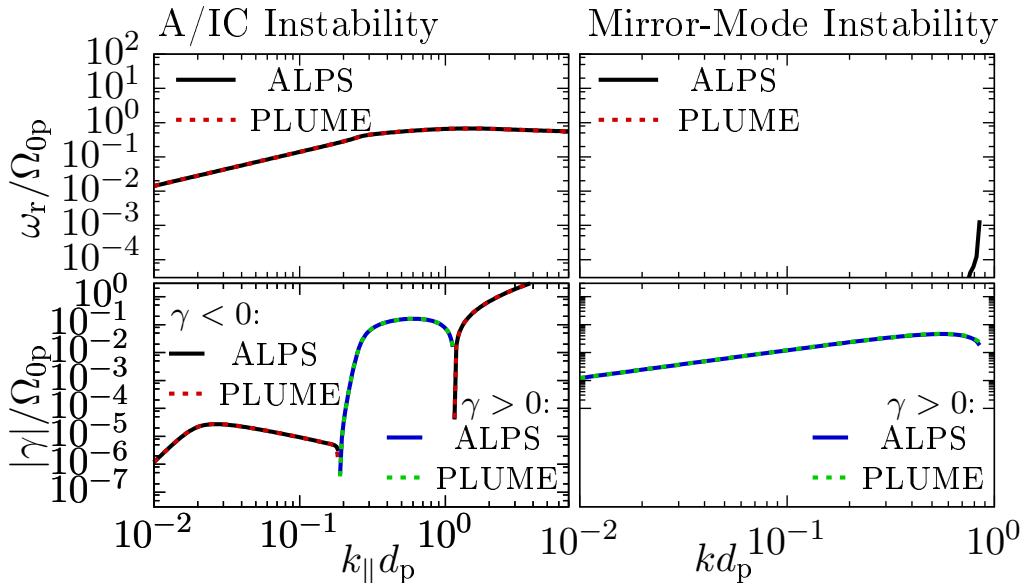


FIGURE 3. Comparison of dispersion relations for the A/IC instability (left) and the mirror-mode instability (right) from PLUME and ALPS. We use $T_{\perp p}/T_{\parallel p} = 3$. For the calculation of the A/IC instability, we keep $k_{\perp}d_p = 10^{-3}$ constant and scan through k_{\parallel} . For the calculation of the mirror-mode instability, we keep $\theta = 75^{\circ}$ constant and scan through $|\mathbf{k}|$.

use PLUME to calculate ω_r and γ as functions of the wavenumber in a plasma with bi-Maxwellian protons and Maxwellian electrons using $\beta_{\parallel p} = \beta_{\parallel e} = \beta_{\perp e} = 1$, $T_{\perp p}/T_{\parallel p} = 3$, and $v_A/c = 10^{-4}$. We then set up bi-Maxwellian f_0 tables with the same parameters and calculate the dispersion relations for both instabilities with ALPS. We show the results in Figure 3. For the ALPS calculation, we use $n_{\perp} = 320$, $n_{\parallel} = 640$, and $P_{\max, \parallel p} = 8m_p v_A$, $P_{\max, \perp p} = 13.9m_p v_A$, $P_{\max, \parallel e} = P_{\max, \perp e} = 0.19m_p v_A$, $J_{\max} = 10^{-45}$, $n_I = 5$, $n_p = 100$, and $T_{\text{lim}} = 0.01$. We study the accuracy of these results depending on the resolution in Appendix A.2.

Both PLUME and ALPS show that the A/IC wave and the mirror mode are unstable in different wave-vector ranges for the given parameter set. The good agreement between the PLUME solutions and the ALPS solutions shows that ALPS successfully calculates the dispersion relations of both instabilities in a bi-Maxwellian plasma.

4.3. Anisotropic κ -Distributions

Astfalk *et al.* (2015) developed the code DSHARK to calculate dispersion relations in plasmas with bi- κ -distributions. As one example, these authors discuss the FM/W instability in an anisotropic electron-proton plasma with $\kappa_p = \kappa_e = 8$, $\beta_{\parallel p} = 2$, $\beta_{\parallel e} = 4$, $T_{\perp p}/T_{\parallel p} = 0.4$, and $T_{\perp e}/T_{\parallel e} = 0.5$ (see Figure 1 from Astfalk *et al.* 2015). The angle between \mathbf{k} and \mathbf{B}_0 is constant for this calculation and set to $\theta = 0.001^{\circ}$. We use DSHARK to reproduce this test case and set up κ -distributed f_0 tables with the same parameters in order to compare the DSHARK results with ALPS. We show this comparison in Figure 4. In ALPS, we use $n_{\perp} = 400$, $n_{\parallel} = 800$, $P_{\max, \parallel p} = 10m_p v_A$, $P_{\max, \perp p} = 6.32m_p v_A$, $P_{\max, \parallel e} = 0.33m_p v_A$, $P_{\max, \perp e} = 0.23m_p v_A$, $J_{\max} = 10^{-45}$, $n_I = 5$, $n_p = 500$, $T_{\text{lim}} = 0.01$, and $v_A/c = 10^{-4}$.

ALPS reproduces the DSHARK results for the FM/W instability well. The results also agree with the previous work by Lazar *et al.* (2011).

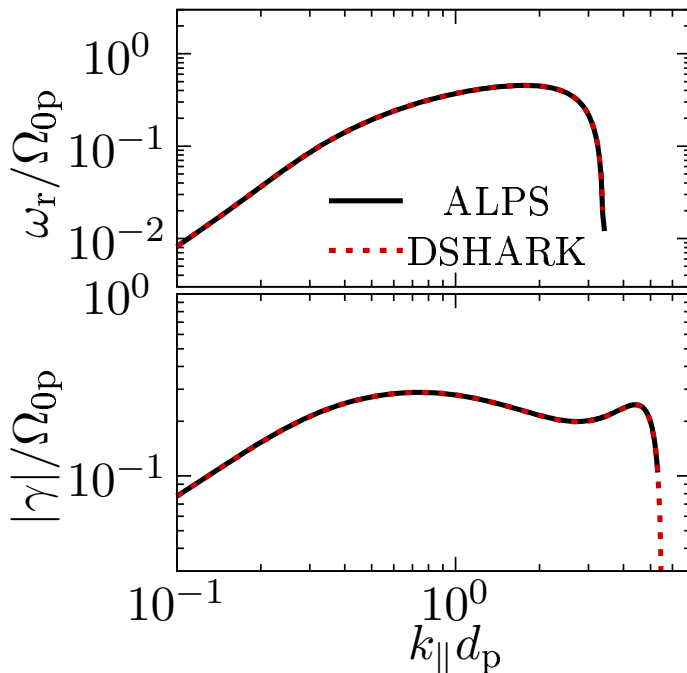


FIGURE 4. Comparison of dispersion relations of the FM/W instability in a κ -distributed plasma from DSHARK and ALPS. In both plasma models, we keep $\theta = 0.001^\circ$ constant and scan through k_{\parallel} . The top panel shows the real part of the wave frequency, and the bottom panel shows its imaginary part.

4.4. Relativistic Jüttner Distributions

As one example for a dispersion relation in a relativistic plasma, we reproduce the results by López *et al.* (2014) for an electron-positron pair plasma with a Jüttner distribution using $v_A/c = 1$, $m_p = m_e$, $\beta_{\parallel p} = \beta_{\parallel e} = (0.2, 0.4, 1.0)$ and $T_{\perp j} = T_{\parallel j}$ for both positrons and electrons. We set up a Jüttner-distributed f_0 table with the same parameters and calculate the dispersion relations of the A/IC wave and the Ordinary wave (O-mode) in the plasma, keeping the perpendicular wavenumber constant at $k_{\perp} d_p = 10^{-3}$. We use $n_{\perp} = 30$, $n_{\parallel} = 60$, $P_{\max} = 5m_p v_A$, $J_{\max} = 10^{-45}$, $n_I = 5$, $n_p = 300$, and $T_{\text{lim}} = 0.01$. Our interpolation method transforms the $(p_{\perp}, p_{\parallel})$ grid to the $(\Gamma, \bar{p}_{\parallel})$ grid with $n_{\Gamma} = 500$ and $n_{\bar{p}_{\parallel}} = 500$ steps in Γ and \bar{p}_{\parallel} , respectively. We show the results in Figure 5. López *et al.* (2014) show their results for these parameters in their Figure 1. Our comparison with the ALPS dispersion relation in Figure 5 shows a good agreement and confirms our relativistic model. The deviation between the results from López *et al.* (2014) and ALPS is only visible in the real part of the frequency at the large- k_{\parallel} /low- ω_r end of the A/IC branches.

5. Discussion and Conclusions

ALPS solves the relativistic and non-relativistic hot-plasma dispersion relations in a plasma with arbitrary background distribution functions. We have benchmarked ALPS against existing codes by comparing dispersion relations for waves and instabilities in Maxwellian, bi-Maxwellian, κ -distributed, and relativistic Jüttner-distributed plasmas.

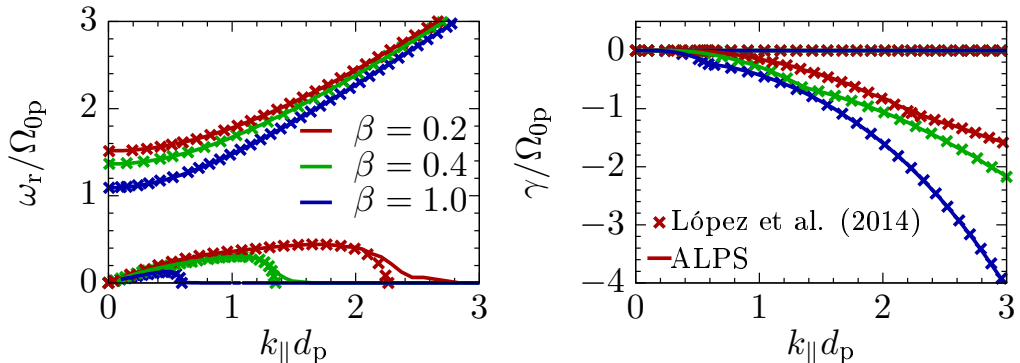


FIGURE 5. Dispersion relations of the quasi-parallel A/IC wave (solutions at low ω_r) and the Ordinary wave (solutions at high ω_r) in a relativistic electron-positron pair plasma with Jüttner distributions. We keep $k_{\perp}d_p = 10^{-3}$ constant and scan through k_{\parallel} . The left panel shows the real part of the frequency, and the right panel shows the imaginary part of the frequency. The lines show ALPS solutions, and the crosses show the results from Figure 1 of López *et al.* (2014). The three colours correspond to $\beta_p = \beta_e = 0.2$ (red), $\beta_p = \beta_e = 0.4$ (green), and $\beta_p = \beta_e = 1.0$ (blue) in both panels and for both modes.

In all cases, we find that ALPS agrees well with existing codes. This finding encourages us to apply ALPS to yet unexplored plasma environments in future work.

An important application of ALPS will be the analysis of distribution functions measured by spacecraft in the solar wind. ALPS includes the necessary numerical framework to preprocess and format the spacecraft data so that they can serve as f_0 tables for direct input (see Appendix C). Especially, the upcoming missions Solar Orbiter and Parker Solar Probe will deliver plasma measurements with unprecedented energy and time resolution in the solar wind that will serve as the ideal input for ALPS. The vast majority of previous kinetic studies of waves and instabilities relied on bi-Maxwellian fits to the observed distribution functions and the use of a standard bi-Maxwellian code to solve the hot-plasma dispersion relation such as WHAMP, NHDS, or PLUME. Our approach allows us, however, to relax the bi-Maxwellian assumption and to analyse the plasma behaviour more realistically. Future comparisons of the results from standard codes such as PLUME with the results from ALPS will help to evaluate the quality of the previous bi-Maxwellian approaches and to refine our understanding of the role of instabilities in collisionless plasmas based on the actual distribution functions. For instance, our knowledge of the realistic value of certain instability thresholds is still very limited. Some in-situ observations of kinetic plasma features in the solar wind lie above the thresholds of kinetic instabilities when calculated based on bi-Maxwellian background distributions (see, for example, Isenberg 2012). The general conjecture is, however, that the plasma is limited by the lowest instability threshold. A more realistic calculation based on the actual distribution functions may resolve this discrepancy. This concept applies, for example, to anisotropy-driven instabilities such as the A/IC instability (Hellinger *et al.* 2006; Bale *et al.* 2009; Maruca *et al.* 2012) or beam-driven instabilities such as the FM/W instability (Reisenfeld *et al.* 2001; Verscharen & Chandran 2013; Verscharen *et al.* 2013a). Also non-thermal electron configurations, which are known to carry a significant heat flux into the solar wind, require a non-bi-Maxwellian representation for the determination of the relevant instabilities that limit their heat flux (Feldman *et al.* 1975; Pilipp *et al.* 1987a; Pulupa *et al.* 2011; Salem *et al.* 2013). Another field of application of ALPS is the study of highly non-thermal plasma configurations related to reconnection events (Phan *et al.*

2006; Gosling 2007; Gosling *et al.* 2007; Egedal *et al.* 2012, 2013). We also emphasise the applicability of ALPS for the determination of dispersion relations using distributions from numerical plasma simulations. Particle-in-cell or Eulerian plasma codes generate data directly suitable as f_0 tables for ALPS. Some of these numerical simulations use (realistically or artificially) relativistic plasma conditions. Therefore, ALPS's ability to include relativistic effects will be very useful for the study of the wave properties and the stability of simulated plasmas.

Our resolution studies in Appendix A offer some insight into the necessary resolution of the f_0 tables for a reliable determination of the plasma dispersion relation. In the shown applications, a minimum resolution of about $n_{\perp} = 40$ and $n_{\parallel} = 80$ has proven to be necessary for a good agreement between ALPS and the test results for (bi-)Maxwellian distributions. In a future extension of ALPS, we will include Nyquist's method to automatically determine the stability of directly observed distribution functions (Klein *et al.* 2017).

We appreciate helpful comments and contributions from Sergei Markovskii and Thomas Brackett. The ALPS collaboration appreciates support from NASA grant NNX16AG81G. We present more details about the numerics on the website www.alps.space. The ALPS source code will be made publicly available on this website after our initial science phase. Computations were performed on Trillian, a Cray XE6m-200 supercomputer at UNH supported by the NSF MRI program under grant PHY-1229408. D.V. was supported by the STFC Ernest Rutherford Fellowship ST/P003826/1. B.D.G.C. was supported in part by NASA grants NNX15AI80G and NNX17AI18G and NSF grant PHY-1500041.

Appendix A. Resolution Studies

In order to understand the required resolution of the f_0 tables for calculations with ALPS, we compare results from PLUME with results from ALPS for the same plasma parameters using different resolutions in this appendix. For all calculations, we use $\beta_{\parallel p} = \beta_{\parallel e} = 1$, $T_{\perp e}/T_{\parallel e} = 1$, $J_{\max} = 10^{-45}$, $n_I = 5$, $n_p = 100$, and $T_{\text{lim}} = 0.01$. We use $P_{\max, \parallel p}$ as a free parameter and set $n_{\parallel} = 2n_{\perp}$, $P_{\max, \parallel e} = P_{\max, \perp e} = P_{\max, \parallel p} \sqrt{m_e/m_p}$, and $P_{\max, \perp p} = P_{\max, \parallel p} \sqrt{T_{\perp p}/T_{\parallel p}}$. We define the resolution in momentum as $\Delta w_j \equiv P_{\max, \parallel j}/(n_{\parallel} m_j w_{\parallel j})$ and the resolution in frequency as $\Delta \omega_r/\omega_r \equiv |\omega_{r, \text{ALPS}} - \omega_{r, \text{PLUME}}|/\omega_{r, \text{PLUME}}$, where $\omega_{r, \text{ALPS}}$ is the solution from ALPS, and $\omega_{r, \text{PLUME}}$ is the solution from PLUME. For κ -distributions, the appropriate resolution depends on both β_j and κ . Instead of giving general guidelines for the resolution, we, therefore, recommend case-by-case convergence studies when calculating dispersion relations in plasmas with κ -distributions.

A.1. Maxwellian Distributions

In Figure 6, we show a resolution study for the A/IC wave in quasi-parallel propagation in an isotropic Maxwellian plasma. This figure complements our solutions shown in Figure 1. The four panels represent different values of $P_{\max, \parallel j}$. In each panel, the diagram at the top compares the real part of the frequency from five ALPS calculations with different Δw_j to the Maxwellian solutions from PLUME. The diagram at the bottom compares the ratio between ω_r from the five ALPS calculations and ω_r from PLUME. In this parameter range, $P_{\max, \parallel p} = 8m_p w_p$ with a resolution finer than $\Delta w_j = 0.1$ leads to a very good agreement with the PLUME solutions for ω_r . For wavenumbers below $1/d_p$, a lower value of $P_{\max, \parallel p}$ is sufficient. Figure 7 shows the same as Figure 6, but giving the

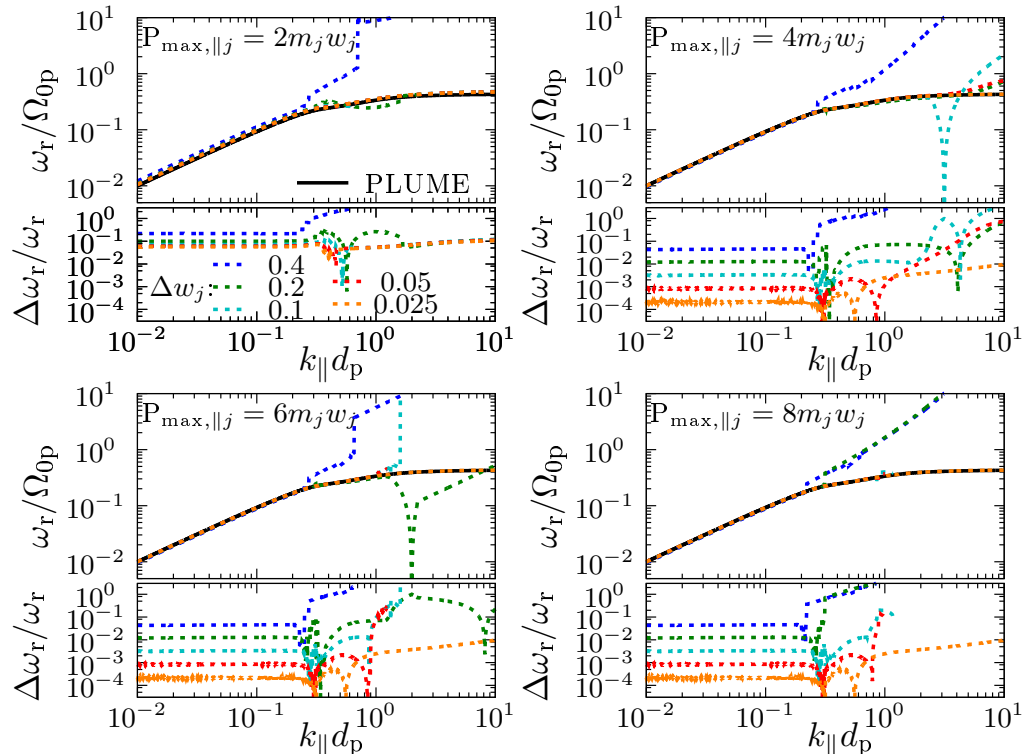


FIGURE 6. Resolution study for the real part of the frequency for the A/IC-wave solution in quasi-parallel propagation. We keep $k_{\perp} d_p = 10^{-3}$ constant and scan through k_{\parallel} .

imaginary part of the frequency instead of its real part. This figure confirms our finding regarding the optimal resolution.

Figures 8 and 9 show the same as Figures 6 and 7, but for quasi-perpendicular propagation instead of quasi-parallel propagation. The required resolution is lower in the quasi-perpendicular case than in the quasi-parallel case. The solutions with $P_{\max, \parallel p} = 4m_p w_p$ and $\Delta w_j \leq 0.1$ lead to a very good agreement between the ALPS and PLUME solutions.

A.2. Anisotropic Bi-Maxwellian Distributions

In addition to our Maxwellian test, we study the dependence of the ALPS solutions on the resolutions for the bi-Maxwellian case with $T_{\perp p}/T_{\parallel p} = 3$ as shown in Figure 3. Figure 10 compares ALPS solutions for the A/IC instability in quasi-parallel propagation for different values of $P_{\max, \parallel p}$ and Δw_j with the solutions from PLUME for the real part of the frequency. Figure 11 compares ALPS and PLUME solutions for the imaginary part of the frequency. The solutions with $P_{\max, \parallel p} = 4m_p w_{\parallel p}$ and $\Delta w_j \leq 0.05$ lead to a good agreement between ALPS and PLUME in both ω_r and γ .

In Figure 12, we study the dependence of the solutions on the resolution for the mirror-mode instability with the same parameters as in Figure 3. The correct solution of the mirror-mode instability has $\omega_r = 0$; however, the ALPS solutions have finite values $\omega_r \neq 0$. The value of ω_r decreases with increasing Δw_j . As Southwood & Kivelson (1993) point out, the mirror-mode instability is strongly influenced by particles with $p_{\parallel} \approx 0$. The error in frequency $\Delta\omega_r$ is determined by the resolution of the momentum grid around

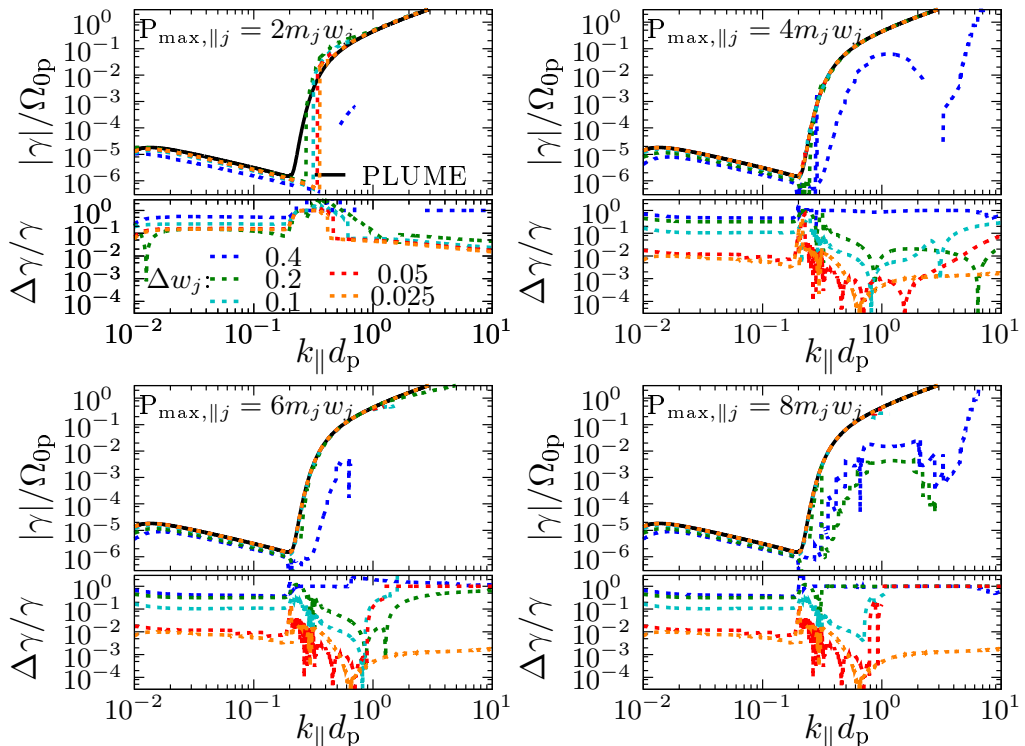


FIGURE 7. Resolution study for the imaginary part of the frequency for the A/IC-wave solution in quasi-parallel propagation. We keep $k_{\perp} d_p = 10^{-3}$ constant and scan through k_{\parallel} .

$p_{\parallel} = 0$, where $\Delta\omega_r \sim k_{\parallel} w_j \Delta w_j$. Figure 13 shows the comparison of the imaginary part of the mirror-mode solutions. Like in the case of the A/IC instability, a resolution with $P_{\max, \parallel p} = 4m_p w_{\parallel p}$ and $\Delta w_j \leq 0.05$ leads to a good agreement between ALPS and PLUME.

Appendix B. Levenberg–Marquardt Fit

For the hybrid analytic continuation, ALPS fits the f_0 table with a combination of pre-described algebraic expressions as described in Section 3.2. We employ a Levenberg–Marquardt algorithm (Levenberg 1944; Marquardt 1963) to fit the distribution functions in p_{\parallel} with a superposition of an arbitrary number of Maxwellian distributions, κ -distributions, and Jüttner distributions. The user can freely choose the number of fits and their superposition. We evaluate different fit parameters for each given value of p_{\perp} . We define the Maxwellian fitting function as

$$F_M(\hat{p}_{\parallel}) = u_1 \exp \left[-y \hat{p}_{\perp} - u_2 (\hat{p}_{\parallel} - u_3)^2 \right], \quad (\text{B1})$$

where u_k are the fit parameters, y is a constant user-defined parameter, and \hat{p}_{\perp} and \hat{p}_{\parallel} are the normalised perpendicular and parallel momenta. The parameter y compensates the otherwise strong p_{\perp} -dependence of u_1 , making the fit more reliable. It is constant for all p_{\perp} . We choose this expression rather than a fit in p_{\perp} since it provides a greater flexibility in the p_{\perp} -domain compared to a two-dimensional fit in p_{\perp} and p_{\parallel} . The best choice for y is $\beta_{\perp j} m_p / m_j$. The standard normalisation in ALPS uses $\hat{p}_{\perp} = p_{\perp} / m_p v_A$

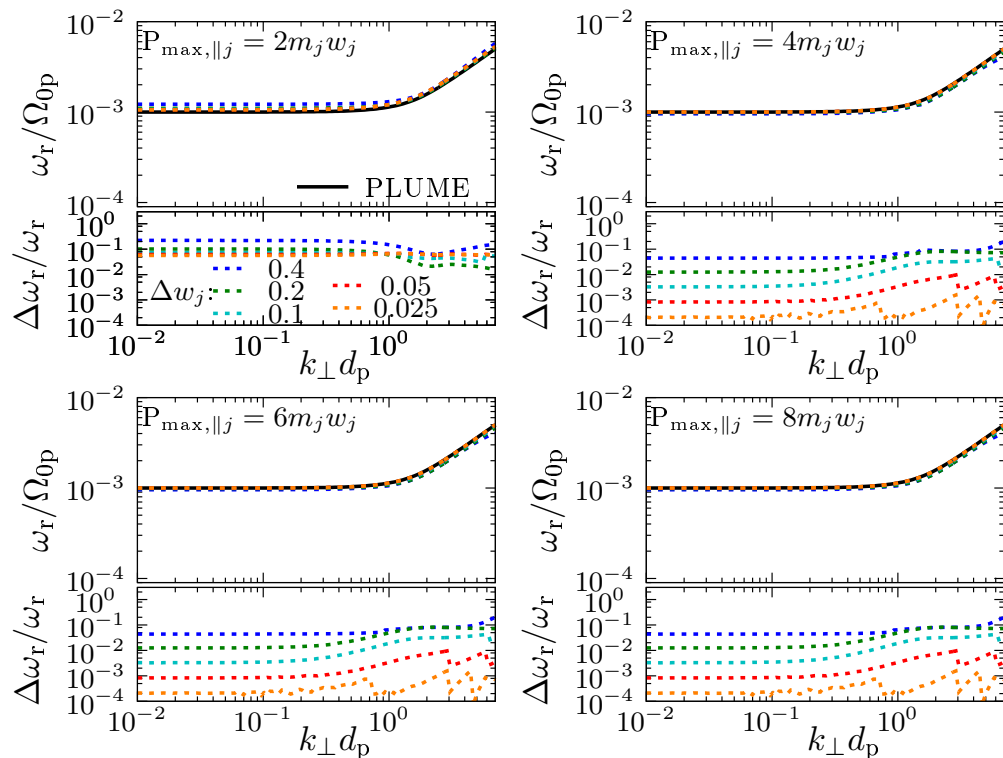


FIGURE 8. Resolution study for the real part of the frequency for the A/IC-wave solution in quasi-perpendicular propagation. We keep $k_{\parallel} d_p = 10^{-3}$ constant and scan through k_{\perp} .

and $\hat{p}_{\parallel} = p_{\parallel} / m_p v_A$. In cases with κ -distributed plasma components, we use

$$F_{\kappa}(\hat{p}_{\parallel}) = u_1 \left[1 + u_2 (\hat{p}_{\parallel} - u_3)^2 + y \hat{p}_{\perp}^2 \right]^{u_4}. \quad (\text{B2})$$

In cases with Jüttner-distributed plasma components, we use

$$F_J = u_1 \exp(-y\Gamma). \quad (\text{B3})$$

In this case, the best choice for y is $2c^2/w_j^2$. These fitting relations are easily extendable by the user to cover more general functions as needed.

We denote the discretised f_0 table of species j at constant p_{\perp} as $\hat{f}_{i,j}(\hat{p}_{\parallel,i})$, the discrete steps in \hat{p}_{\parallel} as $\hat{p}_{\parallel,i}$, the vector of all fit parameters as \mathbf{u} , and the sum of all fit functions as $F(\hat{p}_{\parallel})$. In the Jüttner-distributed cases, the coordinates are replaced with Γ and \bar{p}_{\parallel} accordingly. We define the residuals as $s_i \equiv \hat{f}_{i,j} - F(\hat{p}_{\parallel,i})$ and define $C \equiv \sum_i s_i^2$. We denote the Jacobian of $\hat{\mathbf{f}}_j$ with respect to \mathbf{u} as \mathbf{J} . We use a superposition of analytical expressions for the Jacobian based on the given form of $F(\hat{p}_{\parallel})$.

The Levenberg–Marquardt algorithm uses an iterative step to update \mathbf{u} of the form

$$\mathbf{u}_{\text{new}} = \mathbf{u} + [\mathbf{J}^T \mathbf{J} + \lambda \text{diag}(\mathbf{J}^T \mathbf{J})]^{-1} \mathbf{J}^T \mathbf{s}, \quad (\text{B4})$$

where λ is a user-defined scalar. For the matrix inversion in Equation (B4), we use the **LU**-factorisation. Then we calculate the residuals \mathbf{s}_{new} based on \mathbf{u}_{new} and determine $C_{\text{new}} = |\mathbf{s}_{\text{new}}|^2$. If $C_{\text{new}} \leq C$, we set \mathbf{u} to \mathbf{u}_{new} , reduce λ by a constant factor λ_f (user-defined, standard value is 10), and repeat the procedure. If $C_{\text{new}} > C$, we discard \mathbf{u}_{new} , increase λ by the constant factor λ_f , and repeat the procedure. In this way, we iteratively

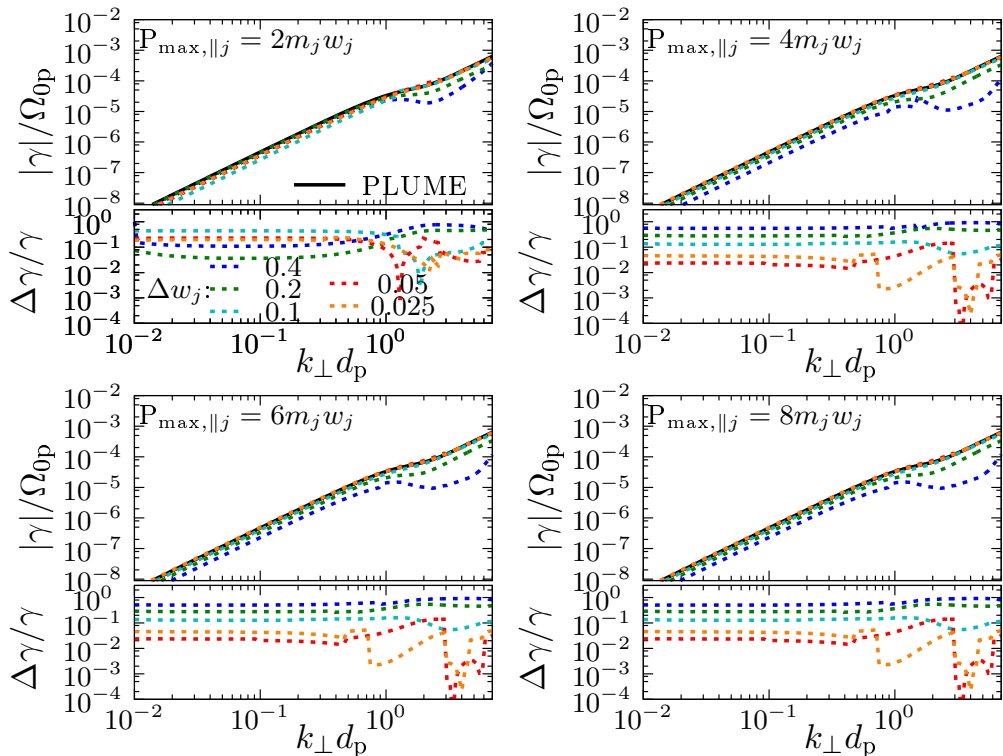


FIGURE 9. Resolution study for the imaginary part of the frequency for the A/IC-wave solution in quasi-perpendicular propagation. We keep $k_{\parallel}d_p = 10^{-3}$ constant and scan through k_{\perp} .

determine the fit parameters \mathbf{u} until the fit converges (i.e., $C \leq \epsilon$ with a user-defined ϵ), or until the number of iterations reaches a user-defined maximum value. ALPS writes the fitted distribution into a separate output file so that a direct comparison with the original input distribution is possible.

Appendix C. The Smoothed Thin-Plate Spline Interpolation

Spacecraft or other plasma data are typically not available on a dense Cartesian grid like the grid required for an f_0 table in ALPS. Therefore, our code includes an interpolation algorithm that fills gaps between data points. ALPS uses the same interpolation algorithm to create an equidistant grid in $(\Gamma, \bar{p}_{\parallel})$ space after the coordinate transformation in cases with relativistic poles. We use a polyharmonic spline interpolation with the radial basis function of a thin-plate spline with smoothing (Powell 1994; Donato & Belongie 2002). For each species, we begin with the “coarse” distribution function $\hat{f}_{c,\mu}$ which is given by n_c data points (index $\mu = 1 \dots n_c$) with the associated coarse momentum coordinates $\hat{p}_{\perp c,\mu}$ and $\hat{p}_{\parallel c,\mu}$. The set $(\hat{f}_{c,\mu}, \hat{p}_{\perp c,\mu}, \hat{p}_{\parallel c,\mu})$ forms one data point. The coarse grid is typically not equally distributed in momentum space.

For each species, the “fine” grid of momentum coordinates is given by $\hat{p}_{\perp,i,k}$ and $\hat{p}_{\parallel,i,k}$ with $i = 1 \dots n_{\perp}$ and $k = 1 \dots n_{\parallel}$ (and correspondingly in the coordinates Γ and \bar{p}_{\parallel} for cases with relativistic poles). The fine grid corresponds to the actual f_0 table to be used as input in ALPS. The goal of our interpolation is to find the value of the distribution function $\hat{f}_{i,k}$ on all grid points (i, k) . We define the vectors $\mathbf{w} = (w_1, \dots, w_{n_c})$, $\mathbf{c} =$

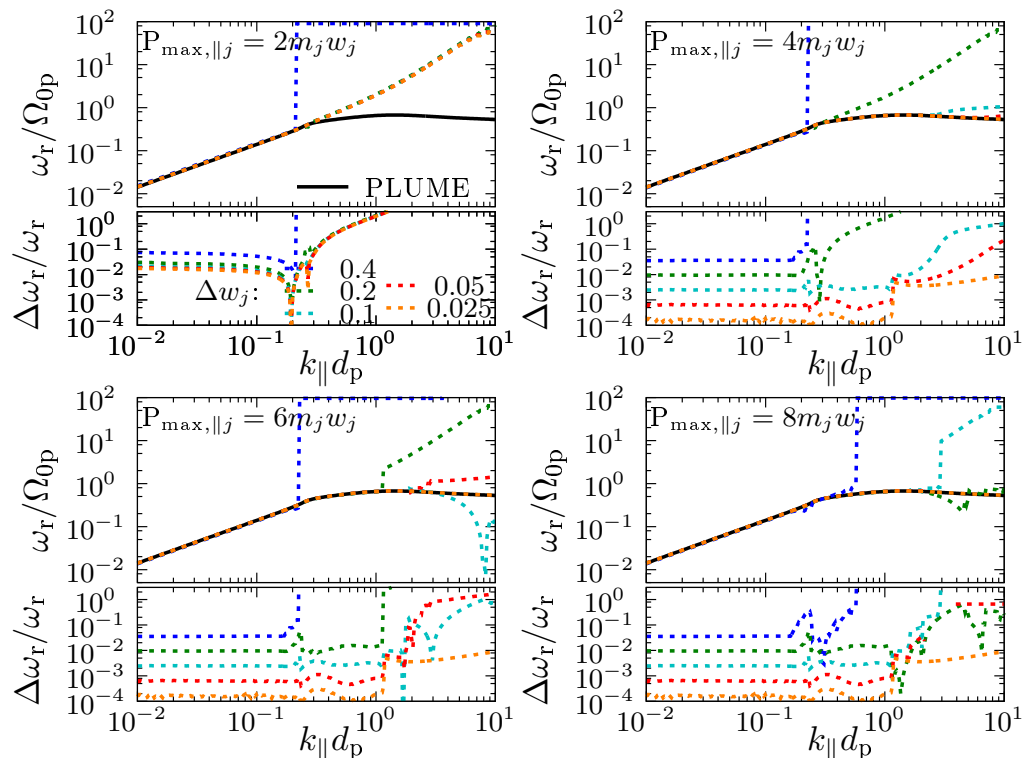


FIGURE 10. Resolution study for the real part of the frequency for the A/IC-instability solution in quasi-parallel propagation. We use a bi-Maxwellian plasma with $T_{\perp p}/T_{\parallel p} = 3$. We keep $k_{\perp} d_p = 10^{-3}$ constant and scan through k_{\parallel} .

(c_1, c_2, c_3) , $\hat{\mathbf{f}}_c = (\hat{f}_{c,1}, \dots, \hat{f}_{c,n_c})$, and $\mathbf{0} = (0, 0, 0)$. We furthermore define the matrix

$$K_{\mu,\nu} = \begin{cases} r^2 \log(r) & \text{if } r \geq 1 \\ r \log(r^r) & \text{if } r < 1, \end{cases} \quad (\text{C1})$$

where $r \equiv \sqrt{(\hat{p}_{\perp c,\mu} - \hat{p}_{\perp c,\nu})^2 + (\hat{p}_{\parallel c,\mu} - \hat{p}_{\parallel c,\nu})^2}$. We also define the $(n_c \times 3)$ matrix \mathbf{P} . Its μ th row is given by $(1, \hat{p}_{\perp c,\mu}, \hat{p}_{\parallel c,\mu})$. The thin-plate spline interpolation requires to solve the nonhomogeneous linear system of equations

$$\left(\begin{array}{c|c} \mathbf{K} + \alpha \mathbf{1} & \mathbf{P} \\ \hline \mathbf{P}^T & 0 \end{array} \right) \left(\begin{array}{c} \mathbf{w} \\ \mathbf{c} \end{array} \right) = \left(\begin{array}{c} \hat{\mathbf{f}}_c \\ \mathbf{0} \end{array} \right) \quad (\text{C2})$$

for the vectors \mathbf{w} and \mathbf{c} . α is a user-defined smoothing parameter ($\alpha = 0$ forces the fine grid to run through all points of the coarse grid), and $\mathbf{1}$ is the $(n_c \times n_c)$ unit matrix. The interpolation is then given by

$$\hat{f}_{i,k} = c_1 + c_2 \hat{p}_{\perp,i,k} + c_3 \hat{p}_{\parallel,i,k} + \sum_{\mu=1}^{n_c} w_{\mu} R_{i,k}^{\mu}, \quad (\text{C3})$$

where $R_{i,k}^{\mu} \equiv \sqrt{(\hat{p}_{\perp,i,k} - \hat{p}_{\perp c,\mu})^2 + (\hat{p}_{\parallel,i,k} - \hat{p}_{\parallel c,\mu})^2}$. The numerically expensive part of the interpolation is the solution of Equation (C2). Since $K_{11} = 0$, a direct **LU** fac-

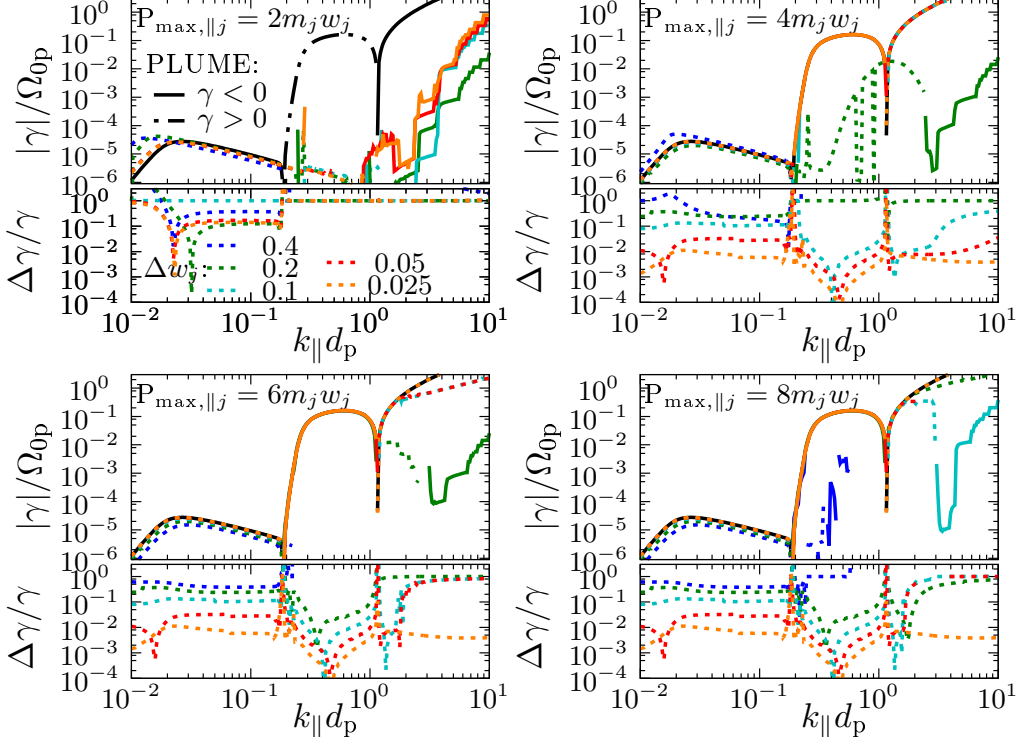


FIGURE 11. Resolution study for the imaginary part of the frequency for the A/IC-instability solution in quasi-parallel propagation. We use a bi-Maxwellian plasma with $T_{\perp p}/T_{\parallel p} = 3$. We keep $k_{\perp} d_p = 10^{-3}$ constant and scan through k_{\parallel} .

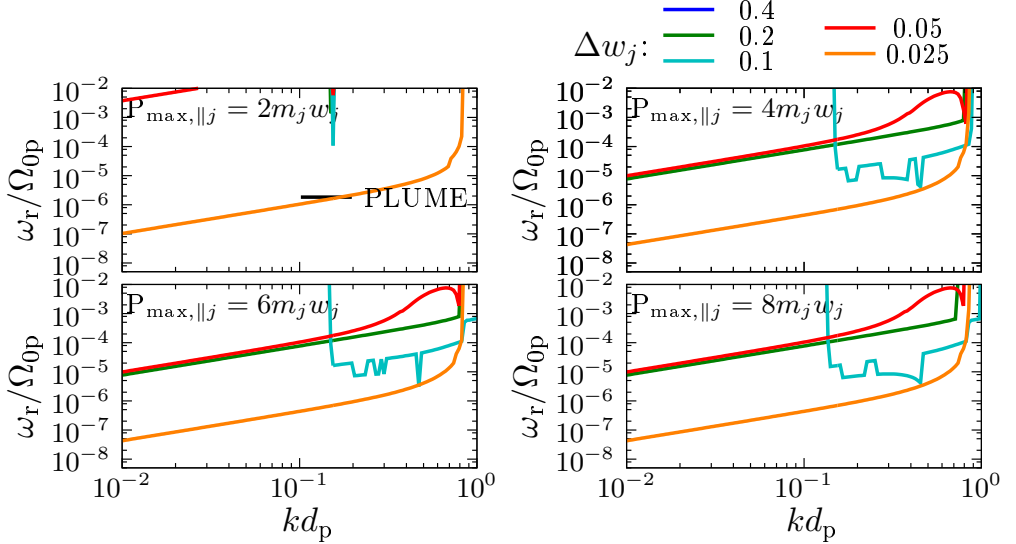


FIGURE 12. Resolution study for the real part of the frequency for the mirror-mode-instability solution. We use a bi-Maxwellian plasma with $T_{\perp p}/T_{\parallel p} = 3$. We keep $\theta = 75^\circ$ constant and scan through $|\mathbf{k}|$.

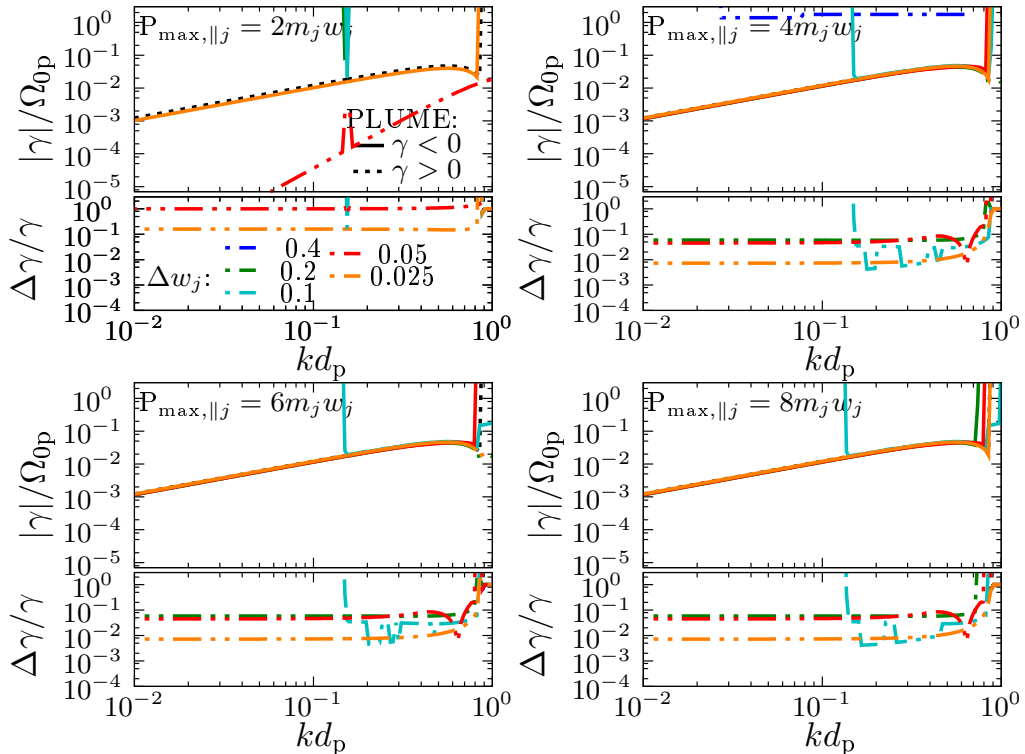


FIGURE 13. Resolution study for the imaginary part of the frequency for the mirror-mode-instability solution. We use a bi-Maxwellian plasma with $T_{\perp p}/T_{\parallel p} = 3$. We keep $\theta = 75^\circ$ constant and scan through $|\mathbf{k}|$.

torisation is not possible. Therefore, we apply a **LU**-factorisation algorithm with partial pivoting through row permutations until $K_{11} \neq 0$.

REFERENCES

- ARMSTRONG, T. P., PAONESSA, M. T., BELL, II, E. V. & KRIMIGIS, S. M. 1983 Voyager observations of Saturnian ion and electron phase space densities. *J. Geophys. Res.* **88**, 8893–8904.
- ASTFALK, PATRICK, GRILER, TOBIAS & JENKO, FRANK 2015 Dshark: A dispersion relation solver for obliquely propagating waves in bi-kappa distributed plasmas. *J. Geophys. Res.* pp. n/a–n/a, 2015JA021507.
- ASTFALK, PATRICK & JENKO, FRANK 2017 Leopard: A grid-based dispersion relation solver for arbitrary gyrotropic distributions. *Journal of Geophysical Research: Space Physics* **122** (1), 89–101, 2016JA023522.
- BALE, S. D., KASPER, J. C., HOWES, G. G., QUATAERT, E., SALEM, C. & SUNDKVIST, D. 2009 Magnetic Fluctuation Power Near Proton Temperature Anisotropy Instability Thresholds in the Solar Wind. *Physical Review Letters* **103** (21), 211101, arXiv: 0908.1274.
- BUTI, B. 1962 Plasma Oscillations and Landau Damping in a Relativistic Gas. *Phys. Fluids* **5**, 1–5.
- CANNON, J. R. & MILLER, KEITH 1965 Some problems in numerical analytic continuation. *J. Soc. Industrial Appl. Math.: Series B, Num. Analysis* **2** (1), 87.
- CATTAERT, T., HELLBERG, M. A. & MACE, R. L. 2007 Oblique propagation of electromagnetic waves in a kappa-Maxwellian plasma. *Physics of Plasmas* **14** (8), 082111.
- CHACÓN-ACOSTA, G., DAGDUG, L. & MORALES-TÉCOTL, H. A. 2010 Manifestly covariant

- Jüttner distribution and equipartition theorem. *Phys. Rev. E* **81** (2), 021126, arXiv: 0910.1625.
- CHRISTON, S. P., MITCHELL, D. G., WILLIAMS, D. J., FRANK, L. A., HUANG, C. Y. & EASTMAN, T. E. 1988 Energy spectra of plasma sheet ions and electrons from about 50 eV/e to about 1 MeV during plasma temperature transitions. *J. Geophys. Res.* **93**, 2562–2572.
- DAVIDSON, R. C. & OGDEN, J. M. 1975 Electromagnetic ion cyclotron instability driven by ion energy anisotropy in high-beta plasmas. *Physics of Fluids* **18**, 1045–1050.
- DAVIS, P. J. & RABINOWITZ, P. 1984 *Methods of numerical integration, Second Edition*.
- DONATO, GIANLUCA & BELONGIE, SERGE 2002 Approximate thin plate spline mappings. In *Proceedings of the 7th European Conference on Computer Vision-Part III*, pp. 21–31. London, UK: Springer-Verlag.
- DUM, C. T., MARSCH, E. & PILIPP, W. 1980 Determination of wave growth from measured distribution functions and transport theory. *J. Plasma Phys.* **23**, 91–113.
- EGEDAL, J., DAUGHTON, W. & LE, A. 2012 Large-scale electron acceleration by parallel electric fields during magnetic reconnection. *Nature* **8**, 321–324.
- EGEDAL, J., LE, A. & DAUGHTON, W. 2013 A review of pressure anisotropy caused by electron trapping in collisionless plasma, and its implications for magnetic reconnection. *Phys. Plasmas* **20** (6), 061201.
- EVIATAR, A. & SCHULZ, M. 1970 Ion-temperature anisotropies and the structure of the solar wind. *Planet. Space Sci.* **18**, 321–332.
- FELDMAN, W. C., ASBRIDGE, J. R., BAME, S. J., MONTGOMERY, M. D. & GARY, S. P. 1975 Solar wind electrons. *J. Geophys. Res.* **80**, 4181–4196.
- FU, C.-L., ZHANG, Y.-X., CHENG, H. & MA, Y.-J. 2012 Numerical analytic continuation on bounded domains. *Engin. Analysis Boundary Elements* **36**, 493.
- FUJIWARA, H., IMAI, H., TAKEUCHI, T. & ISO, Y. 2007 Numerical treatment of analytic continuation with Multiple-precision arithmetic. *Hokkaido Math. J.* **36**, 837.
- GAELZER, R. & ZIEBELL, L. F. 2016 Obliquely propagating electromagnetic waves in magnetized kappa plasmas. *Physics of Plasmas* **23** (2), 022110, arXiv: 1511.05510.
- GAELZER, R., ZIEBELL, L. F. & RAMIRES MENESES, A. 2016 The general dielectric tensor for bi-kappa magnetized plasmas. *ArXiv e-prints*, arXiv: 1605.00279.
- GALVAO, R. A., ZIEBELL, L. F., GAELZER, R. & DE JULI, M. C. 2012 Alfvén waves in dusty plasmas with plasma particles described by anisotropic kappa distributions. *Physics of Plasmas* **19** (12), 123705.
- GARY, S. P. 1993 *Theory of Space Plasma Microinstabilities*.
- GOSLING, J. T. 2007 Observations of Magnetic Reconnection in the Turbulent High-Speed Solar Wind. *Astrophys. J. Lett.* **671**, L73–L76.
- GOSLING, J. T., ASBRIDGE, J. R., BAME, S. J., FELDMAN, W. C., ZWICKL, R. D., PASCHMANN, G., SCKOPKE, N. & HYNDS, R. J. 1981 Interplanetary ions during an energetic storm particle event - The distribution function from solar wind thermal energies to 1.6 MeV. *J. Geophys. Res.* **86**, 547–554.
- GOSLING, J. T., ERIKSSON, S., PHAN, T. D., LARSON, D. E., SKOUG, R. M. & MCCOMAS, D. J. 2007 Direct evidence for prolonged magnetic reconnection at a continuous x-line within the heliospheric current sheet. *Geophys. Res. Lett.* **34**, 6102.
- HARRIS, E. G. 1961 Plasma instabilities associated with anisotropic velocity distributions. *Journal of Nuclear Energy* **2**, 138–145.
- HELLBERG, M., MACE, R. & CATTART, T. 2005 Effects of Superthermal Particles on Waves in Magnetized Space Plasmas. *Space Sci. Rev.* **121**, 127–139.
- HELLINGER, P., TRÁVNÍČEK, P., KASPER, J. C. & LAZARUS, A. J. 2006 Solar wind proton temperature anisotropy: Linear theory and WIND/SWE observations. *Geophys. Res. Lett.* **33**, 9101.
- HELLINGER, P. & TRÁVNÍČEK, P. M. 2011 Proton core-beam system in the expanding solar wind: Hybrid simulations. *J. Geophys. Res.* **116**, 11101.
- HELLINGER, P. & TRÁVNÍČEK, P. M. 2013 Protons and alpha particles in the expanding solar wind: Hybrid simulations. *J. Geophys. Res.* **118**, 5421–5430.
- HUNDHAUSEN, A. J. 1970 Composition and dynamics of the solar wind plasma. *Rev. Geophys. Space Phys.* **8**, 729–811.

- ISENBERG, P. A. 2012 A self-consistent marginally stable state for parallel ion cyclotron waves. *Physics of Plasmas* **19** (3), 032116, arXiv: 1203.1938.
- JÜTTNER, F. 1911 Das Maxwell'sche Gesetz der Geschwindigkeitsverteilung in der Relativtheorie. *Annalen der Physik* **339**, 856–882.
- KLEIN, K. G. & HOWES, G. G. 2015 Predicted impacts of proton temperature anisotropy on solar wind turbulence. *Phys. Plasmas* **22** (3), 032903, arXiv: 1503.00695.
- KLEIN, K. G., HOWES, G. G., TENBARGE, J. M., BALE, S. D., CHEN, C. H. K. & SALEM, C. S. 2012 Using Synthetic Spacecraft Data to Interpret Compressible Fluctuations in Solar Wind Turbulence. *Astrophys. J.* **755**, 159, arXiv: 1206.6564.
- KLEIN, K. G., KASPER, J. C., KORRECK, K. E. & STEVENS, M. L. 2017 Applying Nyquist's method for stability determination to solar wind observations. *J. Geophys. Res.* **122**, 9815–9823.
- KRANICH, S. 2014 Computational analytic continuation. *ArXiv e-prints*, arXiv: 1403.2858.
- LANDAU, L. D. 1946 On the vibrations of the electronic plasma. *J. Phys. (USSR)* **10**, 25–34, [Zh. Eksp. Teor. Fiz. 16,574 (1946)].
- LAZAR, M. & POEDTS, S. 2014 Instability of the parallel electromagnetic modes in Kappa distributed plasmas - II. Electromagnetic ion-cyclotron modes. *Mon. Not. R. Astron. Soc.* **437**, 641–648.
- LAZAR, M., POEDTS, S. & SCHLICKEISER, R. 2011 Proton firehose instability in bi-Kappa distributed plasmas. *Astron. Astrophys.* **534**, A116.
- LAZAR, M. & SCHLICKEISER, R. 2006 Relativistic kinetic dispersion theory of linear parallel waves in magnetized plasmas with isotropic thermal distributions. *New J. Phys.* **8**, 66.
- LAZAR, M. & POEDTS, S. 2009 Firehose instability in space plasmas with bi-kappa distributions. *Astron. Astrophys.* **494**, 311–315.
- LERCHE, I. 1967 Unstable Magnetosonic Waves in a Relativistic Plasma. *Astrophys. J.* **147**, 689.
- LERCHE, I. 1968 Supra-Luminous Waves and the Power Spectrum of an Isotropic, Homogeneous Plasma. *Phys. Fluids* **11**, 413–422.
- LEUBNER, M. P. 1978 Influence of non-bi-Maxwellian distribution function of solar wind protons on the ion cyclotron instability. *J. Geophys. Res.* **83**, 3900–3902.
- LEVENBERG, K. 1944 A method for the solution of certain non-linear problems in least squares. *Quarterly of Applied Mathematics* **2** (2), 164–168.
- LIFSHITZ, E. M. & PITAEVSKII, L. P. 1981 *Physical kinetics*.
- LONGMAN, I. M. 1958 On the numerical evaluation of cauchy principal values of integrals. *Math. Tables Other Aids to Comp.* **12** (63), 205.
- LÓPEZ, R. A., MOYA, P. S., MUÑOZ, V., VIÑAS, A. F. & VALDIVIA, J. A. 2014 Kinetic transverse dispersion relation for relativistic magnetized electron-positron plasmas with Maxwell-Jüttner velocity distribution functions. *Phys. Plasmas* **21** (9), 092107.
- LÓPEZ, R. A., MOYA, P. S., NAVARRO, R. E., ARANEDA, J. A., MUÑOZ, V., VIÑAS, A. F. & ALEJANDRO VALDIVIA, J. 2016 Relativistic Cyclotron Instability in Anisotropic Plasmas. *Astrophys. J.* **832**, 36.
- LUI, A. T. Y. & KRIMIGIS, S. M. 1981 Earthward transport of energetic protons in the earth's plasma sheet. *Geophys. Res. Lett.* **8**, 527–530.
- LUI, A. T. Y. & KRIMIGIS, S. M. 1983 Energetic ion beam in the earth's magnetotail lobe. *Geophys. Res. Lett.* **10**, 13–16.
- MACE, R. L. & SYDORA, R. D. 2010 Parallel whistler instability in a plasma with an anisotropic bi-kappa distribution. *Journal of Geophysical Research (Space Physics)* **115**, 7206.
- MARQUARDT, D. W. 1963 An algorithm for least-squares estimation of nonlinear parameters. *J. Soc. Indust. Appl. Math.* **11** (2).
- MARSCH, E. 2006 Kinetic Physics of the Solar Corona and Solar Wind. *Living Rev. Solar Phys.* **3**, 1.
- MARSCH, E., ROSENBAUER, H., SCHWENN, R., MUEHLHAUSER, K.-H. & NEUBAUER, F. M. 1982a Solar wind helium ions - Observations of the HELIOS solar probes between 0.3 and 1 AU. *J. Geophys. Res.* **87**, 35–51.
- MARSCH, E., SCHWENN, R., ROSENBAUER, H., MUEHLHAUSER, K.-H., PILIPP, W. & NEUBAUER, F. M. 1982b Solar wind protons - Three-dimensional velocity distributions

- and derived plasma parameters measured between 0.3 and 1 AU. *J. Geophys. Res.* **87**, 52–72.
- MARSCH, E. & TU, C.-Y. 2001 Evidence for pitch angle diffusion of solar wind protons in resonance with cyclotron waves. *J. Geophys. Res.* **106**, 8357–8362.
- MARUCA, B. A., KASPER, J. C. & GARY, S. P. 2012 Instability-driven Limits on Helium Temperature Anisotropy in the Solar Wind: Observations and Linear Vlasov Analysis. *Astrophys. J.* **748**, 137.
- MATSUDA, Y. & SMITH, G. R. 1992 A microinstability code for a uniform magnetized plasma with an arbitrary distribution function. *J. Computational Phys.* **100**, 229–235.
- PHAN, T. D., GOSLING, J. T., DAVIS, M. S., SKOUG, R. M., ØIEROSET, M., LIN, R. P., LEPPING, R. P., MCCOMAS, D. J., SMITH, C. W., REME, H. & BALOGH, A. 2006 A magnetic reconnection X-line extending more than 390 Earth radii in the solar wind. *Nature* **439**, 175–178.
- PILIPP, W. G., MUEHLHAUSER, K.-H., MIGGENRIEDER, H., MONTGOMERY, M. D. & ROSENBAUER, H. 1987a Characteristics of electron velocity distribution functions in the solar wind derived from the HELIOS plasma experiment. *J. Geophys. Res.* **92**, 1075–1092.
- PILIPP, W. G., MUEHLHAUSER, K.-H., MIGGENRIEDER, H., ROSENBAUER, H. & SCHWENN, R. 1987b Variations of electron distribution functions in the solar wind. *J. Geophys. Res.* **92**, 1103–1118.
- POWELL, M. J. D. 1994 Some algorithms for thin-plate spline interpolation to functions of two variables. In *H. P. Dikshit and C. A. Micchelli (Eds.): Advances in Computational Mathematics, New Delhi, India*, pp. 303–319. Singapore: World Scientific.
- PRESS, W. H., TEUKOLSKY, S. A., VETTERLING, W. T. & FLANNERY, B. P. 1992 *Numerical recipes in FORTRAN. The art of scientific computing*.
- PULUPA, M., SALEM, C. S., HORAITES, K. I. & BALE, S. 2011 Solar wind electron microphysics: Results from a Wind electron database. *AGU Fall Meeting Abstracts* p. B2034.
- QUATAERT, E. 1998 Particle Heating by Alfvénic Turbulence in Hot Accretion Flows. *Astrophys. J.* **500**, 978, arXiv: arXiv:astro-ph/9710127.
- REICHEL, L. 1986 Numerical methods for analytic continuation and mesh generation. *Constructive Approximation* **2**, 23.
- REISENFELD, D. B., GARY, S. P., GOSLING, J. T., STEINBERG, J. T., MCCOMAS, D. J., GOLDSTEIN, B. E. & NEUGEBAUER, M. 2001 Helium energetics in the high-latitude solar wind: Ulysses observations. *J. Geophys. Res.* **106**, 5693–5708.
- ROBINSON, P. A. 1990 Systematic methods for calculation of the dielectric properties of arbitrary plasmas. *Journal of Computational Physics* **88**, 381–392.
- ROENNMARK, K. 1982 Waves in homogeneous, anisotropic multicomponent plasmas (WHAMP). *Tech. Rep.*
- RUDAKOV, L. I. & SAGDEEV, R. Z. 1961 On the Instability of a Nonuniform Rarefied Plasma in a Strong Magnetic Field. *Soviet Physics Doklady* **6**, 415.
- SALEM, C. S., PULUPA, M., VERSCHAREN, D., BALE, S. D. & CHANDRAN, B. D. 2013 Electron Temperature Anisotropies in the Solar Wind: Properties, Regulation and Constraints. *AGU Fall Meeting Abstracts* p. B2104.
- SCHWARTZ, S. J. 1980 Plasma instabilities in the solar wind - A theoretical review. *Reviews of Geophysics and Space Physics* **18**, 313–336.
- SOUTHWOOD, D. J. & KIVELSON, M. G. 1993 Mirror instability. I - Physical mechanism of linear instability. *J. Geophys. Res.* **98**, 9181–9187.
- STIX, T. H. 1992 *Waves in plasmas*.
- SUMMERS, D. & THORNE, R. M. 1991 The modified plasma dispersion function. *Phys. Fluids B* **3**, 1835–1847.
- SUMMERS, D., XUE, S. & THORNE, R. M. 1994 Calculation of the dielectric tensor for a generalized Lorentzian (κ) distribution function. *Phys. Plasmas* **1**, 2012–2025.
- SWANSON, D. G. 2002 Exact and moderately relativistic plasma dispersion functions. *Plasma Phys. Contr. F.* **44**, 1329–1347.
- TAJIRI, M. 1967 Propagation of Hydromagnetic Waves in Collisionless Plasma. II. Kinetic Approach. *J. Phys. Soc. Japan* **22**, 1482.
- ŠTVERÁK, Š., MAKSIMOVIC, M., TRÁVNÍČEK, P. M., MARSCH, E., FAZAKERLEY, A. N. &

- SCIME, E. E. 2009 Radial evolution of nonthermal electron populations in the low-latitude solar wind: Helios, Cluster, and Ulysses Observations. *J. Geophys. Res.* **114**, A05104.
- VASYLIUNAS, V. M. 1968 A survey of low-energy electrons in the evening sector of the magnetosphere with OGO 1 and OGO 3. *J. Geophys. Res.* **73**, 2839–2884.
- VERSCHAREN, D., BOUROUAINE, S. & CHANDRAN, B. D. G. 2013a Instabilities Driven by the Drift and Temperature Anisotropy of Alpha Particles in the Solar Wind. *Astrophys. J.* **773**, 163, arXiv: 1307.1823.
- VERSCHAREN, D., BOUROUAINE, S., CHANDRAN, B. D. G. & MARUCA, B. A. 2013b A Parallel-propagating Alfvénic Ion-beam Instability in the High-beta Solar Wind. *Astrophys. J.* **773**, 8, arXiv: 1306.2531.
- VERSCHAREN, D. & CHANDRAN, B. D. G. 2013 The Dispersion Relations and Instability Thresholds of Oblique Plasma Modes in the Presence of an Ion Beam. *Astrophys. J.* **764**, 88, arXiv: 1212.5192.
- VERSCHAREN, D., CHANDRAN, B. D. G., KLEIN, K. G. & QUATAERT, E. 2016 Collisionless Isotropization of the Solar-wind Protons by Compressive Fluctuations and Plasma Instabilities. *Astrophys. J.* **831**, 128, arXiv: 1605.07143.
- VERSCHAREN, D., CHEN, C. H. K. & WICKS, R. T. 2017 On Kinetic Slow Modes, Fluid Slow Modes, and Pressure-Balanced Structures in the Solar Wind. *ArXiv e-prints* , arXiv: 1703.03040.
- WEIDEMAN, J. A. C. 1995 Computing the Hilbert transform on the real line. *Math. Comp.* **64**, 745–762.
- WILLIAMS, D. J., MITCHELL, D. G. & CHRISTON, S. P. 1988 Implications of large flow velocity signatures in nearly isotropic ion distributions. *Geophys. Res. Lett.* **15**, 303–306.
- XIE, H.-S. 2013 Generalized plasma dispersion function: One-solve-all treatment, visualizations, and application to Landau damping. *Physics of Plasmas* **20** (9), 092125, arXiv: 1305.6476.
- XUE, S., THORNE, R. M. & SUMMERS, D. 1993 Electromagnetic ion-cyclotron instability in space plasmas. *J. Geophys. Res.* **98**, 17475–17484.
- XUE, S., THORNE, R. M. & SUMMERS, D. 1996 Excitation of magnetosonic waves in the undisturbed solar wind. *Geophys. Res. Lett.* **23**, 2557–2560.
- YOON, P. H., SEOUGH, J. J., KHIM, K. K., KIM, H., KWON, H.-J., PARK, J., PARKH, S. & PARK, K. S. 2010 Analytic model of electromagnetic ion-cyclotron anisotropy instability. *Physics of Plasmas* **17** (8), 082111.
- ZHANG Z.-Q. MA, Y.-J. 2013 A modified kernel method for numerical analytic continuation. *Inverse Prob. Sci. Engin.* **21** (5), 840.